LETTER

Molecular control of macroscopic forces drives formation of the vertebrate hindgut

Nandan L. Nerurkar[1,6,7]*, ChangHee Lee[1], L. Mahadevan[2,3,4,5] & Clifford J. Tabin[1]*

The embryonic gut tube is a cylindrical structure from which the respiratory and gastrointestinal tracts develop[1]. Although the early emergence of the endoderm as an epithelial sheet[2,3] and later morphogenesis of the definitive digestive and respiratory organs[4–6] have been investigated, the intervening process of gut tube formation remains relatively understudied[7,8]. Here we investigate the molecular control of macroscopic forces underlying early morphogenesis of the gut tube in the chick embryo. The gut tube has been described as forming from two endodermal invaginations— the anterior intestinal portal (AIP) towards the rostral end of the embryo and the caudal intestinal portal (CIP) at the caudal end— that migrate towards one another, internalizing the endoderm until they meet at the yolk stalk (umbilicus in mammals)[1,6]. Migration of the AIP to form foregut has been descriptively characterized[8,9], but the hindgut is likely to form by a distinct mechanism that has not been fully explained[10]. We find that the hindgut is formed by collective cell movements through a stationary CIP, rather than by movement of the CIP itself. Further, combining in vivo imaging, biophysics and mathematical modelling with molecular and embryological approaches, we identify a contractile force gradient that drives cell movements in the hindgut-forming endoderm, enabling tissue-scale posterior extension of the forming hindgut tube. The force gradient, in turn, is established in response to a morphogenic gradient of fibroblast growth factor signalling. As a result, we propose that an important positive feedback arises,

whereby contracting cells draw passive cells from low to high fibroblast growth factor levels, recruiting them to contract and pull more cells into the elongating hindgut. In addition to providing insight into the early gut development, these findings illustrate how large-scale tissue level forces can be traced to developmental signals during vertebrate morphogenesis.

To study the process of hindgut formation, we first labelled small populations of endoderm cells in the developing chick embryo at Hamburger–Hamilton stage (HH) 13 (50 h of incubation), when the posterior endoderm is flat, and observed their movement through the completion of hindgut tube formation at HH18 (72 h)[11]. Labelled endodermal cells along the midline were displaced posteriorly through the CIP and internalized in the forming hindgut, outpacing posterior elongation of the embryo (red arrowhead, Fig. 1a); no anterior movement of the CIP was observed. Because the allantois—visible posteriorly as a crescent-shaped invagination (Fig. 1a–c and Extended Data Fig. 1c)— has often been misidentified as the CIP[10,12], we tested whether anterior migration of the allantois could explain internalization of the hindgut endoderm. However, the forming hindgut elongated markedly faster than anterior migration of the allantois (Extended Data Fig. 1a), suggesting that hindgut formation cannot be explained by anterior migration of the CIP or allantois. Because hindgut formation coincides with a posterior shift in the endoderm, we next focused on how these two processes may be related. Cell-labelling experiments revealed that posterior movement of the endoderm outpaced neighbouring mesodermal
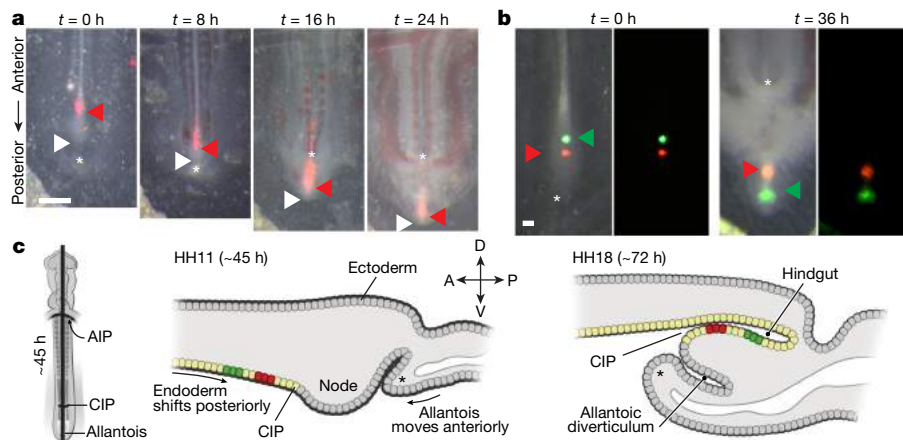

Fig. 1 | The chick hindgut forms by antero-posterior inversion of endoderm passing through the CIP. a, Ventral view of embryo in which endoderm was labelled with the lipophilic membrane dye DiI (red arrow) at HH13 ($t = 0$ h after dye injection). White arrow, posterior tip of embryo; *, allantois; image representative of four chick embryos from four independent experiments. Scale bar, 500 μm. **b**, The lipophilic membrane dyes DiO (green arrow) and DiI (red arrow) injected into midline endoderm at HH11 ($t = 0$ h after dye injection, left) and after incubation

to HH18 ($t = 36$ h, right). Image representative of 4 chick embryos from 4 independent experiments. *, allantoic lip. Scale bar, 100 μm. **c**, Schematic of hindgut formation: endoderm folds from dorsal to ventral, inverting cell positions (red- and green-labelled cells) along the antero-posterior axis as cells move through a stationary CIP. The ventral lip of the allantois (*) migrates in a posterior to anterior direction. A, anterior; P, posterior; D, dorsal; V, ventral.

[1]Department of Genetics, Harvard Medical School, Boston, MA, USA. [2]School of Engineering and Applied Sciences, Harvard University, Cambridge, MA, USA. [3]Department of Organismic and Evolutionary Biology, Harvard University, Cambridge, MA, USA. [4]Department of Physics, Harvard University, Cambridge, MA, USA. [5]Kavli Institute for Bionano Science and Technology, Harvard University, Cambridge, MA, USA. [6]Department of Biomedical Engineering, Columbia University, New York, NY, USA. [7]Department of Genetics and Development, Columbia University Medical Center, New York, NY, USA. *e-mail: nln2113@columbia.edu; tabin@genetics.med.harvard.edu
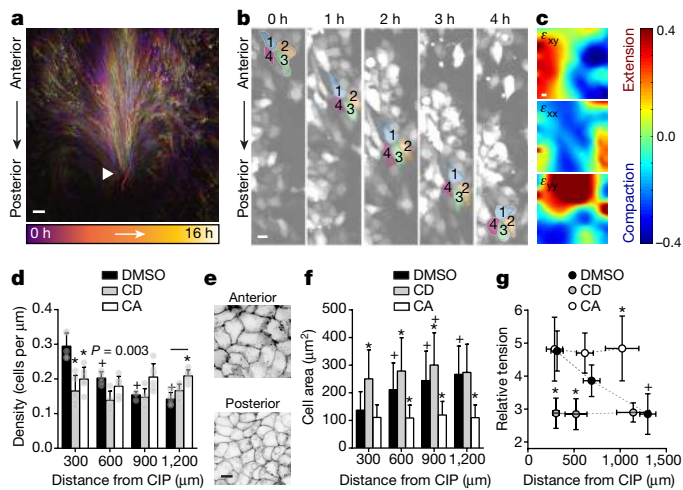
Fig. 2 | A contractile gradient drives polarized collective cell movements to form hindgut. a, Cell tracks from a time-lapse experiment representative of 8 chick embryos from 8 independent experiments from HH14 (purple, $t = 0$ h) to HH18 (white, $t = 16$ h). White arrowhead, CIP. Scale bar, 100 μm. **b**, Time-lapse (original magnification, $40\times$) snapshots of four neighbouring endoderm cells; representative of collective movements from three chick embryos from three independent experiments. Scale bar, 10 μm. **c**, Representative heat maps of shear strain (ε_{xy}, top), medio-lateral strain (ε_{xx}, middle) and antero-posterior strain (ε_{yy}, bottom) for 8-h time lapse (HH14 to HH16). Colour bar (right) indicates magnitude of the strain. See schematic in Extended Data Fig. 3a for details. **d**, Linear cell density at HH15 following treatment with 0.1% DMSO ($n = 5$ embryos), 5 μM cytochalasin D (CD; $n = 5$ embryos) or 30 nM calyculin A (CA; $n = 6$ embryos). At least 900 cells were counted per embryo; data are mean ± s.d.; two-way ANOVA with Tukey's correction; *$P \leq 0.001$ versus DMSO; +$P \leq 0.001$ versus posterior-most bin for the respective treatment. **e**, Ventral–apical view of anterior (top) and posterior (bottom) endoderm at HH15, stained with the lipophilic dye PKH26 to visualize cell boundaries; representative of three chick embryos from three individual experiments (see Extended Data Fig. 3c). Scale bar, 10 μm. **f**, Cell area at HH15 following treatment with 0.1% DMSO ($n = 7$ embryos), 5 μM cytochalasin D ($n = 7$ embryos) or 30 nM calyculin A ($n = 6$ embryos). At least 800 cells were counted per embryo; data are mean ± s.d.; two-way ANOVA with Tukey's correction; *$P \leq 0.001$ versus DMSO; +$P \leq 0.001$ versus posterior-most bin for the respective treatment. **g**, Relative tension at HH15 following treatment with 0.1% DMSO ($n = 27$ embryos, 8–10 per group), 5 μM cytochalasin D ($n = 30$ embryos, 10 per group) or 30 nM calyculin A ($n = 26$ embryos, 8–9 per group); mean ± s.d.; one-way ANOVA with Tukey's correction; *$P \leq 0.001$ versus DMSO; +$P \leq 0.001$ versus posterior-most bin for the respective treatment.

derivatives (Extended Data Fig. 1b), suggesting that the endoderm is not simply displaced passively with mesoderm as the embryo elongates, but instead actively moves posteriorly. Focusing next on movements within the endoderm, we found that the relative position of labels injected into the flat endoderm at HH11 became inverted along the antero-posterior axis once they had been internalized to form hindgut by HH18 (Fig. 1b). On the basis of these findings, we suggest a model for hindgut formation in which endoderm cells rapidly pass through the relatively stationary CIP and, because these movements outpace axis elongation, they are accommodated in the growing tail bud by dorso-ventral folding (Fig. 1c). This model contradicts the prior view that anterior migration of the CIP zips the endoderm into a tube as it moves, yet is entirely consistent with fate-mapping studies in the chick and mouse[13–16].

To directly observe cell movements during hindgut formation, we performed endoderm-specific electroporation of a ubiquitous GFP reporter in the ex ovo chick embryo (Extended Data Fig. 1c–e), followed by live in vivo imaging of cell movements between HH14 and HH18. We observed collective anterior-to-posterior cell movements along the embryonic midline (Fig. 2a, and Supplementary Video 1), with cells passing through the CIP and out of view. Live imaging

following dual electroporation of endoderm and mesoderm confirmed that cell movements were intrinsic to endoderm (Supplementary Video 2). We observed minimal cell proliferation (Extended Data Fig. 1f) or neighbour exchange (Fig. 2b and Supplementary Video 3) in the posterior endoderm, indicating that proliferation-based growth and intercalary or convergent-extension movements are unlikely to drive the observed movements.

Because they are required for hindgut formation (Extended Data Fig. 1g, h), we next focused on understanding mechanistically how these collective movements occur in the endoderm, which forms a polarized epithelium before tube morphogenesis (Extended Data Fig. 2). In general, it is not clear how collective cell movements are coordinated in embryonic epithelia in the absence of a 'leader' population[17]. Therefore, we sought to understand biophysically how cells move collectively during hindgut formation. To do so, we tracked cell movements in the posterior endoderm and calculated mechanical strain to quantify endoderm stretching, compaction and shearing during hindgut formation[18] (Fig. 2c and Extended Data Fig. 3a). Strain (ε) is a unitless metric for changes in shape of a material, calculated from the spatial gradient in cell displacements[19] (see Supplementary Methods for a detailed description). Along the antero-posterior axis (the direction of collective cell movement), we observed neighbouring regions of posterior compaction ($\varepsilon_{yy} < 0$) and anterior extension ($\varepsilon_{yy} > 0$, Fig. 2c and Extended Data Fig. 4a). Compaction strains posteriorly coincided with increased cell density (Extended Data Fig. 3b) and a decreased cell area (Fig. 2e and Extended Data Fig. 3c). These opposing gradients of cell density and shape were lost upon either pharmacologic disruption or enhancement of actomyosin contractility (Fig. 2d, f). Cell height varied inversely with area (Extended Data Fig. 3d), suggesting that cells undergo volume-persevering changes in cell shape as they move from a region of extensional strain in the anterior endoderm to compaction strain in the posterior endoderm. These data suggest either that anterior endoderm expands to push cells posteriorly, or that posterior cells contract to pull anterior cells into the forming hindgut. To distinguish between these two possibilities, we measured relative forces within the endoderm, using a Gastromaster device to perform cuts of reproducible geometry, and measuring the degree to which cuts spring open as a measure of tension[18,20] (see Supplementary Methods and Extended Data Fig. 3e–g). In the posterior endoderm, where cells are compacted together during collective movement, cuts rapidly opened to 4.76 ± 0.64 times their original size ($n = 10$), indicating that the compacting tissue is under tension. Therefore, the posterior endoderm is not pushed, but instead contracts to pull anterior cells into the forming hindgut. The coincidence of tensile forces and compaction strains in the posterior endoderm also suggests that the propulsive force for cell movements is intrinsic to these cells and is not extrinsically applied, such as by an unseen migratory 'leader' population[21]. Measurement of tension along the antero-posterior axis revealed a tensional gradient, with endoderm tension decreasing from posterior to anterior (Extended Data Fig. 3h). Disruption and activation of actomyosin contractility resulted in a loss of the tensional gradient due to a reduction in posterior tension and increase in anterior tension, respectively (Fig. 2g and Extended Data Fig. 3i). This suggests that the spatial gradient of endoderm tension is a result of actomyosin contraction.

Disrupting cell contractility using cytochalasin D treatment caused a reduction in cell movements and associated antero-posterior strains (Extended Data Fig. 5b, e and Supplementary Video 4). Increasing contractility by treating endoderm with calyculin A reversed the direction of cell movements (Extended Data Fig. 5c and Supplementary Video 4) and induced large extensional strains throughout the endoderm (Extended Data Fig. 5f). These data suggest that spatial differences in cell contractility generate the tensional gradient that drives collective movements to form the hindgut tube.

These studies provide a macroscopic picture of the physical basis of collective cell movements in the posterior endoderm and the forces responsible. We next sought to identify the molecular cues by which these forces are prescribed. Fibroblast growth factor (FGF) signalling
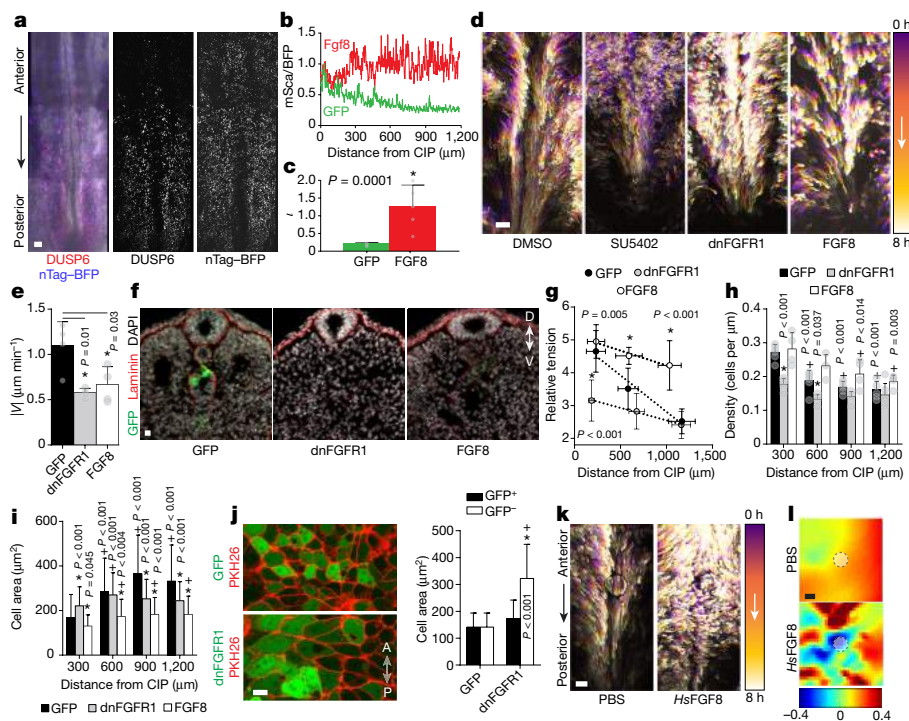
Fig. 3 | A posterior FGF8 gradient modulates endoderm tensional gradient to control collective cell movements. a, Co-electroporation of DUSP6–mScarlet reporter and control CAG-nuclear (n)TagBFP ($n = 7$). Scale bar, 100 μm. **b, c,** DUSP6–mScarlet (mSca) reporter activity normalized to CAG-nTag BFP (**b**) and gradient shape parameter ι (**c**; GFP, green, $n = 7$ embryos; FGF8: red, $n = 5$ embryos); data are mean ± s.d.; unpaired two-tailed t-test. **d,** Representative cell tracks (HH14 to HH16) of embryos electroporated with GFP in 0.1% DMSO (cell tracks affected in $n = 0$ of 3 chick embryos) or 50 μM SU5402 ($n = 3/3$ affected), or electroporated with dnFGFR1-IRES-GFP or FGF8-IRES-GFP. Scale bar, 100 μm. **e,** Mean cell velocity ($n = 4$ embryos per condition). Data are mean ± s.d.; one-way ANOVA with Tukey's correction. **f,** Transverse sections through posterior of HH18 embryos. All 5 GFP-electroporated embryos formed hindgut, versus 3 of 12 embryos electroporated with dnFGFR1-IRES-GFP and 8 of 21 embryos electroporated with FGF8-IRES-GFP. D, dorsal; V, ventral. Scale bar, 10 μm. **g,** Relative tension at HH15, $n = 10$ embryos per condition; data are mean ± s.d.; one-way ANOVA with Tukey's correction; *$P < 0.05$ versus GFP-only control. **h, i,** Cell density (**h**; ≥1,000 cells from each embryo electroporated with GFP only ($n = 6$), dnFGFR1-IRES-GFP ($n = 6$) or FGF8-IRES-GFP ($n = 4$)) and area (**i**; ≥1,000 cells from each embryo electroporated with GFP only ($n = 6$), dnFGFR1-IRES-GFP ($n = 7$) or FGF8-IRES-GFP ($n = 8$)) at HH15. Data are mean ± s.d.; two-way ANOVA with Tukey's correction; *$P < 0.05$ versus GFP-only control, +$P < 0.05$ versus posterior-most bin per treatment. **j,** Membrane stain PKH26, showing mosaic expression of GFP (top) and dnFGFR1-IRES-GFP (left) at HH15. Cell area (right) of GFP+ and GFP− cells following electroporation with GFP (197 cells, $n = 3$ embryos) or dnFGFR1-IRES-GFP (209 cells, $n = 4$ embryos). Data are mean ± s.d.; two-way ANOVA with Tukey's correction; *$P < 0.05$ versus GFP only, +$P < 0.05$ versus dnFGFR1-IRES-GFP. **k,** Cell tracks (HH14 to HH16) with anteriorly grafted beads soaked with PBS (0 of 3 embryos exhibit disrupted tracks) or with HsFGF8 (4 of 7 embryos show disrupted tracks). Scale bar, 100 μm. **l,** Heat maps of ε_{yy} for embryos with anteriorly grafted beads soaked with PBS (1 of 5 embryos show ectopic compaction strains) or with HsFGF8 (4 of 6 embryos show ectopic compaction strains). The bead is marked by a white circle. Scale bar, 100 μm.

modulates actomyosin activity in several developmental contexts[22–26], and *FGF8* is expressed in a posterior-to-anterior gradient (Extended Data Fig. 6a) that is central to posterior mesodermal[24,27] and ectodermal[28] morphogenesis. However, a role for FGF signalling in posterior endoderm morphogenesis has not previously been explored. We therefore tested whether this pathway has a role in coordinating the collective cell movements that lead to hindgut tube formation. Using an FGF reporter that consists of the mouse *Dusp6* promoter driving expression of mScarlet, we observed a gradient in FGF activity specifically within the endoderm[29] (Fig. 3a–c and Extended Data Fig. 9). FGF-target gene expression and downstream signalling were also enriched in the posterior endoderm (Extended Data Fig. 6b–d).

To test for a function of FGF signalling during hindgut morphogenesis, we first used SU5402 to broadly inhibit FGF activity pharmacologically. SU5402 disrupted endoderm cell movements and hindgut formation (Fig. 3d, Extended Data Fig. 6e and Supplementary Video 5), suggesting a general role for FGF signalling. When a dominant negative form of the FGF receptor FGFR1 (dnFGFR1-IRES-GFP) was electroporated exclusively into the endoderm[26], cell movements were similarly reduced (Fig. 3d and Supplementary Video 6), demonstrating that FGF signalling is required specifically within the endoderm for hindgut morphogenesis. We next tested the effects of exogenous activation of the pathway by expressing FGF8 (FGF8-IRES-GFP) throughout the

posterior endoderm. This misexpression of FGF8 phenocopied dnF-GFR1, markedly reducing cell movements (Fig. 3d and Supplementary Video 6). Despite a reduction in mean cell velocity (Fig. 3e) and loss of posterior compaction strains (Extended Data Fig. 4), the degree of coordination among neighbouring cell movements did not depend on FGF (Extended Data Fig. 6h). This suggests that reduced cell movements are likely to result from a change in tissue-level forces, rather than loss of mechanical coordination among neighbouring cells. Disruption of cell movements by misexpression of dnFGFR1 and FGF8 ultimately resulted in failure to form the hindgut (Fig. 3f).

To understand why activation and inhibition of FGF signalling have similar effects, disrupting collective cell movements and hindgut formation, we investigated whether altering the FGF gradient causes concomitant changes in the tensional gradient. Indeed, inhibition of FGF signalling by expression of dnFGFR1 decreased tension in the posterior endoderm, whereas FGF8 misexpression significantly increased tension in the anterior endoderm (Fig. 3g). Consequently, both dnFGFR1 and FGF8 result in a loss of the tensional gradient driving cell movements. Further, recombinant human FGF8 protein (HsFGF8) increased endoderm tension independently of new protein synthesis (Extended Data Fig. 7b, c). Opposing gradients of cell density and shape were also disrupted (Fig. 3h, i), and posterior compaction strains were diminished (Extended Data Fig. 4b, c) by changes in
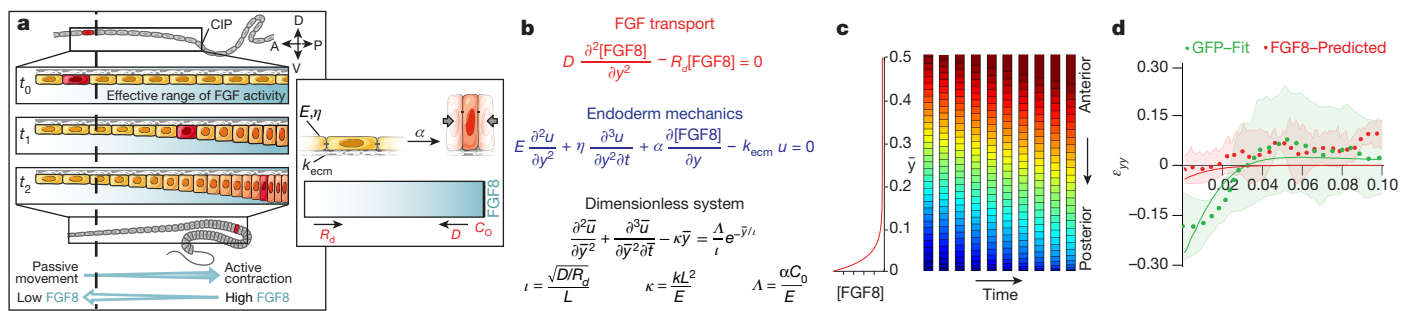
Fig. 4 | A one-dimensional quantitative mechanochemical model for an FGF8-mediated contractile gradient mechanism that causes collective cell movements. a, **b**, Model schematic (**a**) and formulation (**b**, see Supplementary Methods for details). Initial condition $\bar{u}(\bar{y}, 0) = 0$ and boundary conditions $\bar{u}(0, \bar{t}) = \bar{u}(1, \bar{t}) = 0$, where $\bar{y}$ and $\bar{u}$ are antero-posterior position and displacement normalized to domain size L, respectively. E, cellular modulus; η, cellular viscosity; k_{ecm}, stiffness of extracellular matrix; α, contractility constant; D, FGF8 diffusion coefficient; R_d, FGF8 clearance rate; C_o, maximum FGF8 concentration. **c**,

Simulation based on the model ($\iota = 0.03$, $\kappa = 1$, $\Lambda = 1$), with FGF8 distribution (left) and snapshots of resulting endoderm movements (right; colour indicates position $\bar{y}$ at the beginning of simulation). Blue, posterior; red, anterior. **d**, Least-squares curve fit ($R^2 = 0.88$) of model (green line) to experimentally measured strain following electroporation with GFP (green dots), and model prediction (red line) of experimentally measured strain following electroporation with FGF8-IRES-GFP (red dots); shading indicates standard deviation. Experimental data ($n = 3$ embryos) repeated from Extended Data Fig. 4.

FGF signalling. FGF-dependent shape changes were cell-autonomous (Fig. 3j), indicating that cell shape is determined by sensing of FGF signal, and not by the cell's location within the tissue. Grafting of beads soaked with *Hs*FGF8 onto anterior endoderm, in which FGF activity is low and only extensional strains are usually present, disrupted cell movements (Fig. 3k) and induced ectopic zones of compaction (Fig. 3l). Immunofluorescence revealed an FGF-dependent posterior enrichment of active GTP-bound and total RhoA in the posterior endoderm (Extended Data Fig. 8a–f). These results suggest that hindgut formation relies on direct conversion of a spatial gradient in FGF signalling to a mechanical force gradient through modulation of RhoA-dependent actomyosin activity.

Finally, we developed a minimal mathematical model to quantify this mechanism in terms of physico-chemical parameters associated with FGF transport and force balance, and to potentially investigate behaviours of the system that are not experimentally accessible. The formulation (Fig. 4a, b) and solution of the model are described in detail in Supplementary Methods. The endoderm is modelled as an active one-dimensional viscoelastic solid, the movement of which is resisted by an elastic basement membrane (Fig. 4a, inset). Forces in the endoderm are assumed to be the sum of passive viscoelastic and active contractile forces. We assumed that contractility varies linearly with FGF concentration, and FGF ligand diffuses from a posterior source with uniform rate of clearance. This gives rise to a linear partial differential equation for cell displacement as a function of time and space (Fig. 4b), which depends on three dimensionless parameters: a length scale ratio (ι) that relates the diffusion or clearance of FGF ligand to the size of the domain; a ratio of basement membrane stiffness to cell stiffness (κ); and a ratio of contractile to elastic stress (Λ, Fig. 4b).

Model simulations replicate the experimental observations of directional cell movements with posterior compaction and anterior extension (Fig. 4c, Extended Data Fig. 10 and Supplementary Video 7). As cells move from anterior to posterior, their exposure to FGF (and consequently their contractility) increase, resulting in a positive feedback: passive cells become contractile as they are displaced posteriorly, contributing to a further increase in pulling forces on more anterior cells (Fig. 4a). This is analogous to a game of tug of war in which one team, as they begin to win, recruit players from the opposing team. As a result, posterior-directed cell movements extend well beyond the signalling range of FGF8 (Fig. 4c), even when parameter values are altered by multiple orders of magnitude. This may explain why collective cell movement of the endoderm outpaces axis elongation (Fig. 1a, Extended Data Fig. 1b and Supplementary Video 2), despite the fact that both processes are coordinated by the same FGF gradient[24,30]. This feedback behaviour, inferred from the mathematical model, could not

be tested directly by experiment but is consistent with experimental observations.

To apply the model to experimental results, we first measured the gradient shape parameter ($\iota = 0.21 \pm 0.03$, $n = 6$) using the *Dusp6* reporter, then fit the model to experimentally measured strain ε_{yy} to generate values for κ and Λ (green, Fig. 4d). We next tested whether the model can successfully predict the outcome of FGF8 misexpression experiments by changing only the experimentally measured parameter ι (Fig. 3b, c). The model prediction agreed qualitatively with the experiment (Fig. 4d). Therefore, the minimal mathematical model supports the diffusible activator-driven contractile gradient mode of cell movements.

The present work reframes our view of how the gut tube forms, but is nevertheless congruent with fate-mapping studies of chick gut formation, going back to the elegant carbon particle-based mapping experiments described in the doctoral thesis of N. Le Douarin[7]. FGF8 has been implicated in a broad range of events during development. The present work may provide insight into its diverse functions; in different contexts, FGF8 can behave as a chemorepellent[31], a chemoattractant[26] or simply as a mediator of motility[24]. Cells of the presomitic mesoderm are free to move autonomously and a gradient in FGF-mediated acto-myosin activity translates to a gradient in cell motility[24], whereas in the endoderm (where epithelial cells are constrained by cell junctions) we show that this same gradient instead creates collective movements. Therefore, an intriguing possibility is that at the cellular level, FGF signalling acts similarly in each system as a modulator of actomyosin activity, and that the difference in the respective cell movements that result is a physical consequence of differences in cell–cell contacts and tissue constraints.

Reporting summary

Further information on experimental design is available in the Nature Research Reporting Summary linked to this article.

Code availability

All code including model implementation and data processing were written and compiled in MATLAB. Code can be accessed by contacting the authors.

Data availability

Source data for Figs. 1–4 and Extended Data Figs. 1–10 are available in the online version of the paper.

Online content

Any methods, additional references, Nature Research reporting summaries, source data, statements of data availability and associated accession codes are available at https://doi.org/10.1038/s41586-018-0865-9.

1. Gilbert, S. F. *Developmental Biology* 9th edn (Sinauer Associates, Sunderland, 2010).
2. Kwon, G. S., Viotti, M. & Hadjantonakis, A. K. The endoderm of the mouse embryo arises by dynamic widespread intercalation of embryonic and extraembryonic lineages. *Dev. Cell* **15**, 509–520 (2008).
3. Keller, R. Cell migration during gastrulation. *Curr. Opin. Cell Biol.* **17**, 533–541 (2005).
4. Shyer, A. E., Huycke, T. R., Lee, C., Mahadevan, L. & Tabin, C. J. Bending gradients: how the intestinal stem cell gets its home. *Cell* **161**, 569–580 (2015).
5. Kim, H. Y. et al. Localized smooth muscle differentiation is essential for epithelial bifurcation during branching morphogenesis of the mammalian lung. *Dev. Cell* **34**, 1–8 (2015).
6. Zorn, A. M. & Wells, J. M. Vertebrate endoderm development and organ formation. *Annu. Rev. Cell Dev. Biol.* **25**, 221–251 (2009).
7. Le Douarin, N. M. Etude expérimentale de l'organogenèse du tube digestif et du foie chez l'embryon de poulet. PhD thesis, Université Paris (1964).
8. Stalsberg, H. & DeHaan, R. L. Endodermal movements during foregut formation in the chick embryo. *Dev. Biol.* **18**, 198–215 (1968).
9. Seidl, W. & Steding, G. Topogenesis of the anterior intestinal port. Microkinematographic investigations on chick embryos. *Anat. Embryol. (Berl.)* **155**, 37–45 (1978).
10. Gruenwald, P. Normal and abnormal detachment of body and gut from the blastoderm in the chick embryo, with remarks on the early development of the allantois. *J. Morphol.* **69**, 83–125 (1941).
11. Hamburger, V. & Hamilton, H. L. A series of normal stages in the development of the chick embryo. *J. Morphol.* **88**, 49–92 (1951).
12. Bellairs, R. & Osmond, M. *Atlas of Chick Development* 3rd edn (Academic Press, Cambridge, 2014).
13. Rosenquist, G. C. The location of the pregut endoderm in the chick embryo at the primitive streak stage as determined by radioautographic mapping. *Dev. Biol.* **26**, 323–335 (1971).
14. Lawson, K. A., Meneses, J. J. & Pedersen, R. A. Cell fate and cell lineage in the endoderm of the presomite mouse embryo, studied with an intracellular tracer. *Dev. Biol.* **115**, 325–339 (1986).
15. Matsushita, S. Fate mapping study of the endoderm in the posterior part of the 1.5-day-old chick embryo. *Dev. Growth Differ.* **41**, 313–319 (1999).
16. Franklin, V. et al. Regionalisation of the endoderm progenitors and morphogenesis of the gut portals of the mouse embryo. *Mech. Dev.* **125**, 587–600 (2008).
17. Friedl, P. & Gilmour, D. Collective cell migration in morphogenesis, regeneration and cancer. *Nat. Rev. Mol. Cell Biol.* **10**, 445–457 (2009).
18. Varner, V. D., Voronov, D. A. & Taber, L. A. Mechanics of head fold formation: investigating tissue-level forces during early development. *Development* **137**, 3801–3811 (2010).
19. Taber, L. A. *Nonlinear Theory of Elasticity : Applications in Biomechanics* (World Scientific, Singapore, 2004).
20. Zamir, E. A. & Taber, L. A. On the effects of residual stress in microindentation tests of soft tissue structures. *J. Biomech. Eng.* **126**, 276–283 (2004).
21. Lecaudey, V., Cakan-Akdogan, G., Norton, W. H. J. & Gilmour, D. Dynamic Fgf signaling couples morphogenesis and migration in the zebrafish lateral line primordium. *Development* **135**, 2695–2705 (2008).
22. Ernst, S. et al. Shroom3 is required downstream of FGF signalling to mediate proneuromast assembly in zebrafish. *Development* **139**, 4571–4581 (2012).
23. Sai, X. et al. FGF signaling regulates cytoskeletal remodeling during epithelial morphogenesis. *Curr. Biol.* **18**, 976–981 (2008).
24. Bénazéraf, B. et al. A random cell motility gradient downstream of FGF controls elongation of an amniote embryo. *Nature* **466**, 248–252 (2010).
25. Harding, M. J. & Nechiporuk, V. Fgfr–Ras–MAPK signaling is required for apical constriction via apical positioning of Rho-associated kinase during mechanosensory organ formation. *Development* **139**, 3467–3467 (2012).
26. Sato, A. et al. FGF8 signaling is chemotactic for cardiac neural crest cells. *Dev. Biol.* **354**, 18–30 (2011).
27. Dubrulle, J., McGrew, M. J. & Pourquié, O. FGF signaling controls somite boundary position and regulates segmentation clock control of spatiotemporal *Hox* gene activation. *Cell* **106**, 219–232 (2001).
28. Mathis, L., Kulesa, P. M. & Fraser, S. E. FGF receptor signalling is required to maintain neural progenitors during Hensen's node progression. *Nat. Cell Biol.* **3**, 559–566 (2001).
29. Yu, S. R. et al. Fgf8 morphogen gradient forms by a source-sink mechanism with freely diffusing molecules. *Nature* **461**, 533–536 (2009).
30. Dubrulle, J. & Pourquié, O. *fgf8* mRNA decay establishes a gradient that couples axial elongation to patterning in the vertebrate embryo. *Nature* **427**, 419–422 (2004).
31. Yang, X., Dormann, D., Münsterberg, A. E. & Weijer, C. J. Cell movement patterns during gastrulation in the chick are controlled by positive and negative chemotaxis mediated by FGF4 and FGF8. *Dev. Cell* **3**, 425–437 (2002).

Author contributions N.L.N. and C.J.T. conceived and designed experiments. C.L. cloned the DUSP6 reporter and performed *sprouty1* in situ hybridizations with assistance from N.L.N. All other experiments (including vital dye injections, electroporations, live imaging, immunofluorescence and tension measurements) and analysis of those experiments were carried out by N.L.N. under the supervision of C.J.T. The mathematical model was formulated, solved and interpreted by N.L.N. and L.M. The manuscript was prepared by N.L.N. and revised by N.L.N., C.L., L.M. and C.J.T.

**Competing interests** The authors declare no competing interests.

Additional information
Extended data is available for this paper at https://doi.org/10.1038/s41586-018-0865-9.
Supplementary information is available for this paper at https://doi.org/10.1038/s41586-018-0865-9.
Reprints and permissions information is available at http://www.nature.com/reprints.
**Correspondence and requests for materials** should be addressed to N.L.N. or C.J.T.
Publisher's note: Springer Nature remains neutral with regard to jurisdictional claims in published maps and institutional affiliations.
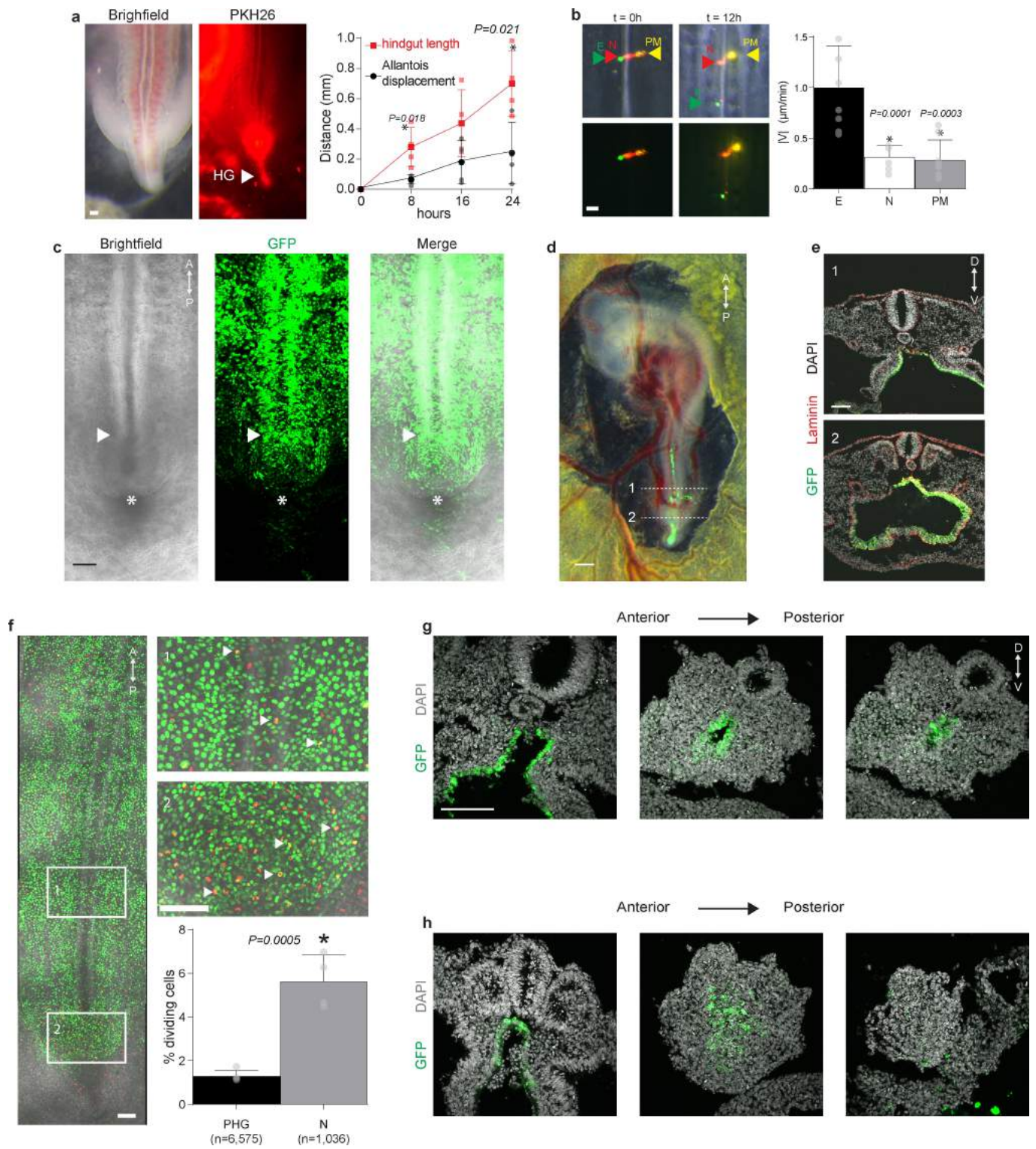
Extended Data Fig. 1 | See next page for caption.

Extended Data Fig. 1 | Electroporation-based transfection of the chick endoderm. a, Dorsal view of HH18 embryo (left) stained with PHK26 to visualize hindgut (HG), and quantification (right) of gut length and allantois displacement from HH14 ($t = 0$ h, $n = 4$ embryos). Data are mean ± s.d.; unpaired t-test. Scale bar, 100 μm. **b**, DiO (green arrow), DiI (red arrow) and DiA (yellow arrow) injected into endoderm (E), notochord (N) and paraxial mesoderm (PM), respectively (image representative of 5 embryos from 5 independent experiments) upon injection at HH14 ($t = 0$ h) and at $t = 12$ h (left), and quantification of antero-posterior velocity (right, $n = 8$ embryos (endoderm, paraxial mesoderm) and $n = 7$ embryos (notochord)). Data are mean ± s.d.; one-way ANOVA with Sidak corrections. *$P < 0.05$ versus endoderm. Scale bar, 100 μm. **c**, Ventral view of posterior HH14 embryo following endoderm-specific electroporation with GFP reporter plasmid at HH12 (image representative of ten embryos from ten independent experiments). White arrowhead, CIP; *, ventral lip of the allantois. Scale bar, 100 μm. **d**, HH18 embryo following endoderm-specific electroporation with GFP reporter plasmid; image representative of eight embryos from eight independent experiments. GFP expression can be seen extending from presumptive midgut endoderm, which remains ventrally open (1), into the hindgut, which has been internalized (2) and extends to the tip of the tail bud. Scale bar, 500 μm. **e**, Transverse sections through the posterior HH18 embryo of GFP-electroporated embryo as indicated in **d**; representative

images from five chick embryos in five individual experiments. Scale bar, 100 μm. **f**, To test whether cell proliferation could provide a contributing force to collective cell movements, endoderm proliferation was quantified by colocalization of phospho-histone H3 immunofluorescence (red) with electroporation-based endodermal expression of H2B–GFP (green). Boxes, enlarged at right, correspond to presumptive hindgut (PHG) endoderm (1), and node-adjacent endoderm (N) (2). Quantification indicates that ~1% of PHG cells are mitotic, suggesting that cell division is not likely to be a major contributor to collective movements. Cell numbers are as indicated from $n = 4$ embryos. Data are mean ± s.d.; unpaired two-tailed t-test; *$P < 0.05$ versus PHG. Scale bar, 100 μm. **g**, **h**, To test whether cell movements are required for hindgut formation, we physically blocked these movements by insertion of a tantalum foil barrier into the endoderm of GFP-electroporated embryos at HH14. In control embryos, in which barrier insertion at an anterior location permitted posterior cell movements, the hindgut formed normally: GFP-expressing cells formed a hollow epithelial tube extending into the tail bud, as indicated in sections from anterior to posterior (left to right) through the HH18 tailbud (**g**; 3 of 3 embryos formed hindgut). However, when the barrier was inserted posteriorly, blocking endoderm movements through the CIP, hindgut formation was disrupted, despite continued outgrowth of the tail bud (**h**; 1 of 4 embryos formed hindgut) Scale bar, 100 μm.
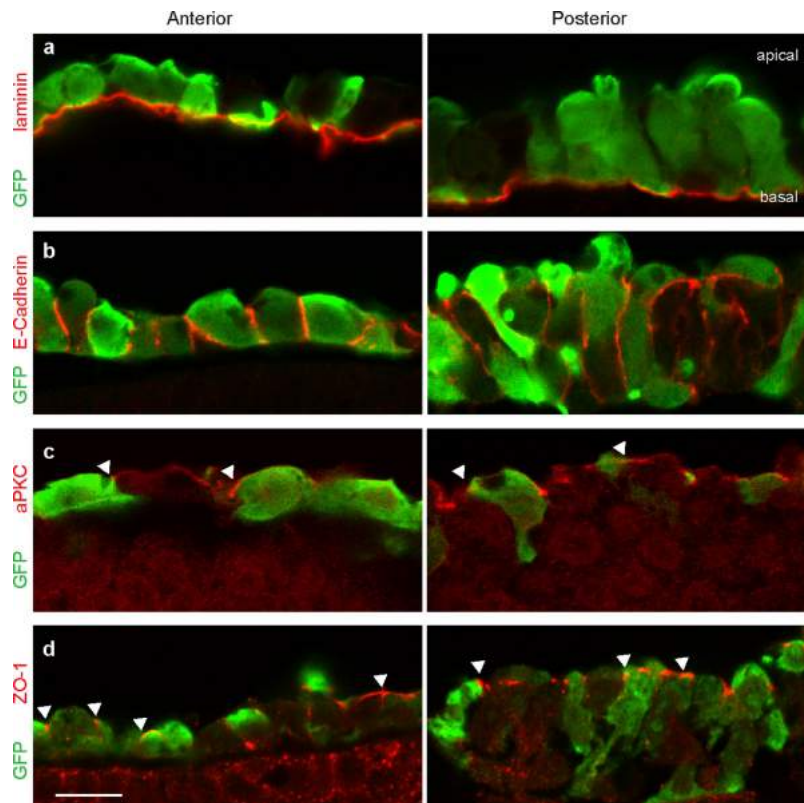
Extended Data Fig. 2 | Immunofluorescent detection of polarized epithelial markers in the definitive endoderm. a–d, Preceding gut tube formation, the endoderm exhibits several hallmarks of a polarized epithelium, including a laminin-rich basement membrane (**a**), basolateral E-cadherin (**b**), and apical localization of aPKC (**c**) and ZO-1 (**d**). Endoderm was visualized by electroporation with GFP, and staining was performed in anterior (left) and posterior (right) endoderm. White arrowheads, apical or junctional localization (image representative of 3 embryos from 3 independent experiments). Scale bar, 10 μm.
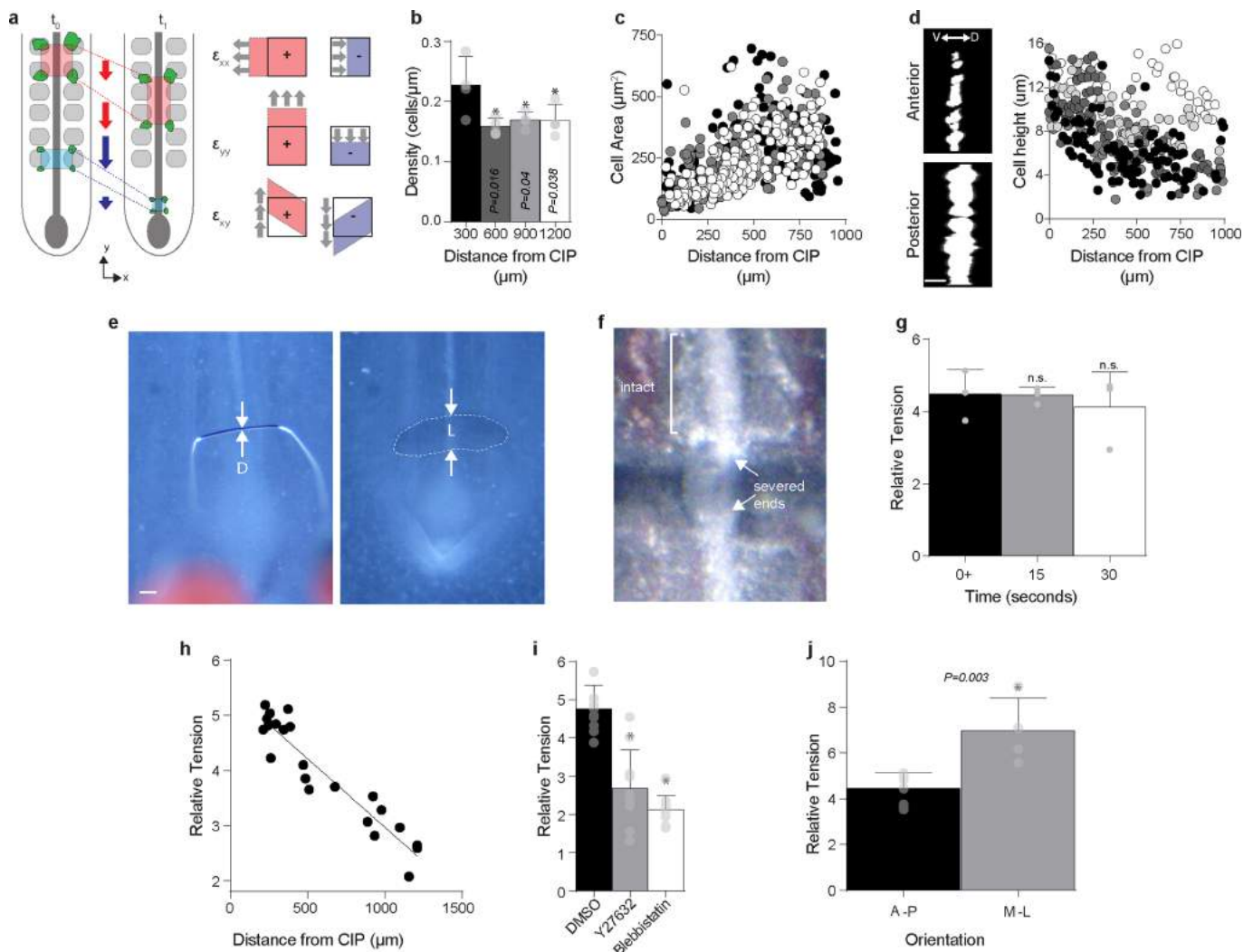
Extended Data Fig. 3 | An endodermal contraction gradient based on relative tension measurements. a, Schematic of strain calculation from cell movements (left) and physical interpretation of the two-dimensional strain components ε_{xy}, ε_{xx} and ε_{yy} (right). x and y axes coincide with medio-lateral and antero-posterior embryonic axes, respectively. At the cellular level, stretching (positive strains) and compaction (negative strains) in a continuous epithelial sheet may be achieved by changes in cell shape or cell–cell contacts that result in an increase or decrease in the distance between centroids of neighbouring cells, respectively. See Supplementary Methods for details of the computation and interpretation of strains in the context of active materials. **b**, Linear cell density in posterior HH15 endoderm ($n = 871$ cells from 4 embryos). Data are mean ± s.d.; one-way ANOVA with Dunnett's correction; *$P < 0.05$ versus posterior-most bin. **c**, Correlation of cell area with antero-posterior position; Pearson's two-tailed coefficient, $r = 0.55$; $n = 616$ cells from 3 embryos; each circle and colour indicates one cell and embryo, respectively. **d**, Dorso-ventral (baso-apical) view of GFP-electroporated cells in the anterior (top left) and posterior (bottom left) endoderm, and negative correlation of cell height with position (right); Pearson's two-tailed coefficient $r = 0.48$; $n = 522$ cells from 5 embryos; each circle and

colour indicates one cell and embryo, respectively. Scale bar, 10 μm. **e**, HH15 posterior embryo in contact with Gastromaster tip, diameter D (left), and following local endoderm ablation (right), which creates a cut of size L (dashed line). Relative tension was measured as the ratio L/D. Scale bar, 100 μm. **f**, Severed notochord visible following Gastromaster ablation. Samples in which the notochord was cut in addition to the endoderm were not included in the analysis. **g**, Relative tension measured over time after cutting at $t = 0$ ($n = 3$ embryos). Wound-healing response was initiated within 1–2 min, decreasing cut size (not shown). Data are mean ± s.d.; one-way ANOVA with Tukey's correction; NS, not significant versus $t = 0$. **h**, Negative correlation of relative tension in wild-type HH15 posterior endoderm with position. Pearson's two-tailed correlation, $r = 0.94$, $n = 22$ embryos. **i**, Relative posterior tension at HH15 is significantly reduced following treatment with 100 μM Y-27632 (Rho kinase inhibitor) or 100 μM blebbistatin (non-muscle myosin inhibitor), when compared to treatment with 0.1% DMSO ($n = 10$ embryos each). Data are mean ± s.d.; one-way ANOVA with Tukey's correction; *$P < 0.001$ versus 0.1% DMSO. **j**, Comparison between relative tension along antero-posterior (A-P, $n = 7$ embryos) and medio-lateral (M-L, $n = 4$ embryos) axes. Data are mean ± s.d.; unpaired two-tailed t-test.
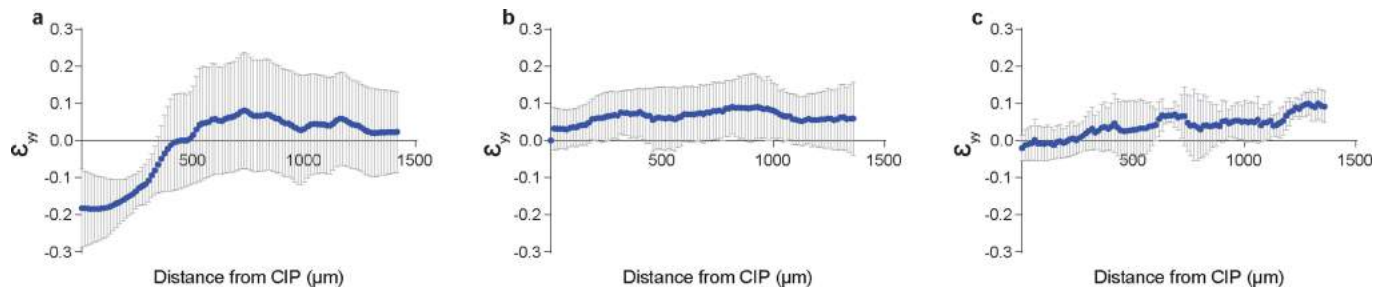
Extended Data Fig. 4 | Antero-posterior morphogenetic strains in the hindgut-forming endoderm. a–c, Average antero-posterior strain ε_{yy} ($n = 3$ embryos, mean ± s.d.) versus position for embryos electroporated with GFP (**a**), dnFGFR1-IRES-GFP (**b**) or FGF8-IRES-GFP (**c**). Large negative (compaction) strains observed in embryos electroporated with GFP were eliminated upon misexpression of dnFGFR1 or FGF8.
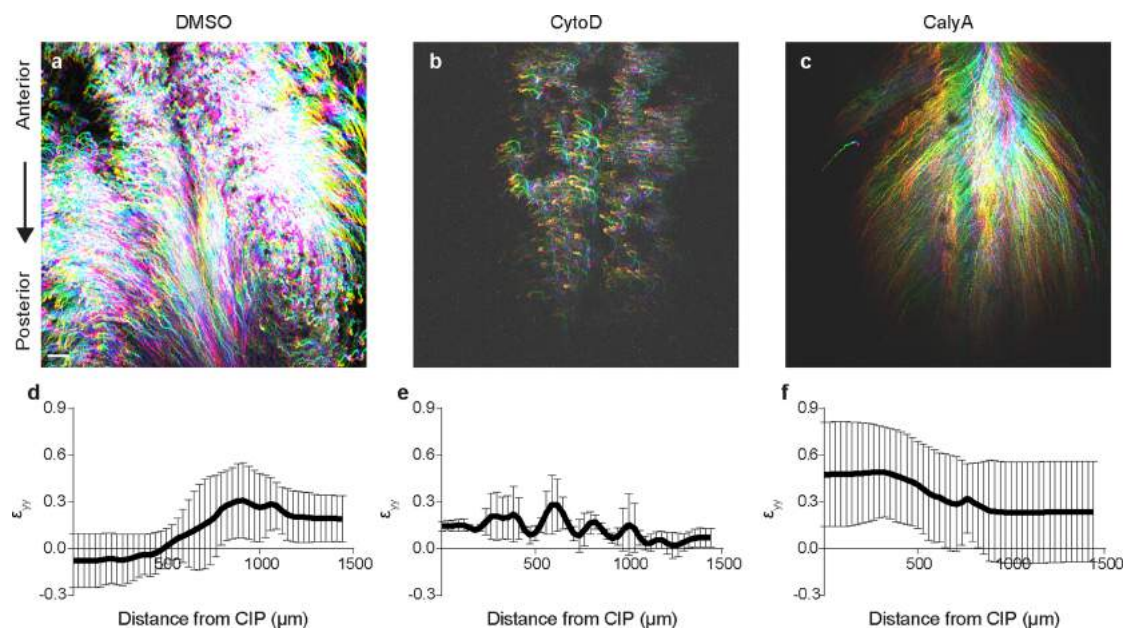
Extended Data Fig. 5 | Endoderm cell movements and strains are disrupted with inhibition and activation of actomyosin contractility. **a–c**, Representative cell tracks (HH14 to HH16) in embryos electroporated with GFP and exposed to 0.1% DMSO (**a**; 0 of 3 embryos affected), 2.5 μM cytochalasin D to disrupt actomyosin activity (**b**; 3 of 3 embryos affected), or 20 nM calyculin A to uniformly increase myosin activity (**c**; 3 of 3 embryos affected). Scale bar, 100 μm. **d–f**, Average antero-posterior strain ε_{yy} ($n = 3$ embryos, mean ± s.d.) versus position from time-lapse experiments for embryos electroporated with GFP and treated with 0.1% DMSO (**d**), 2.5 μM cytochalasin D (**e**) or 20 nM calyculin A (**f**).
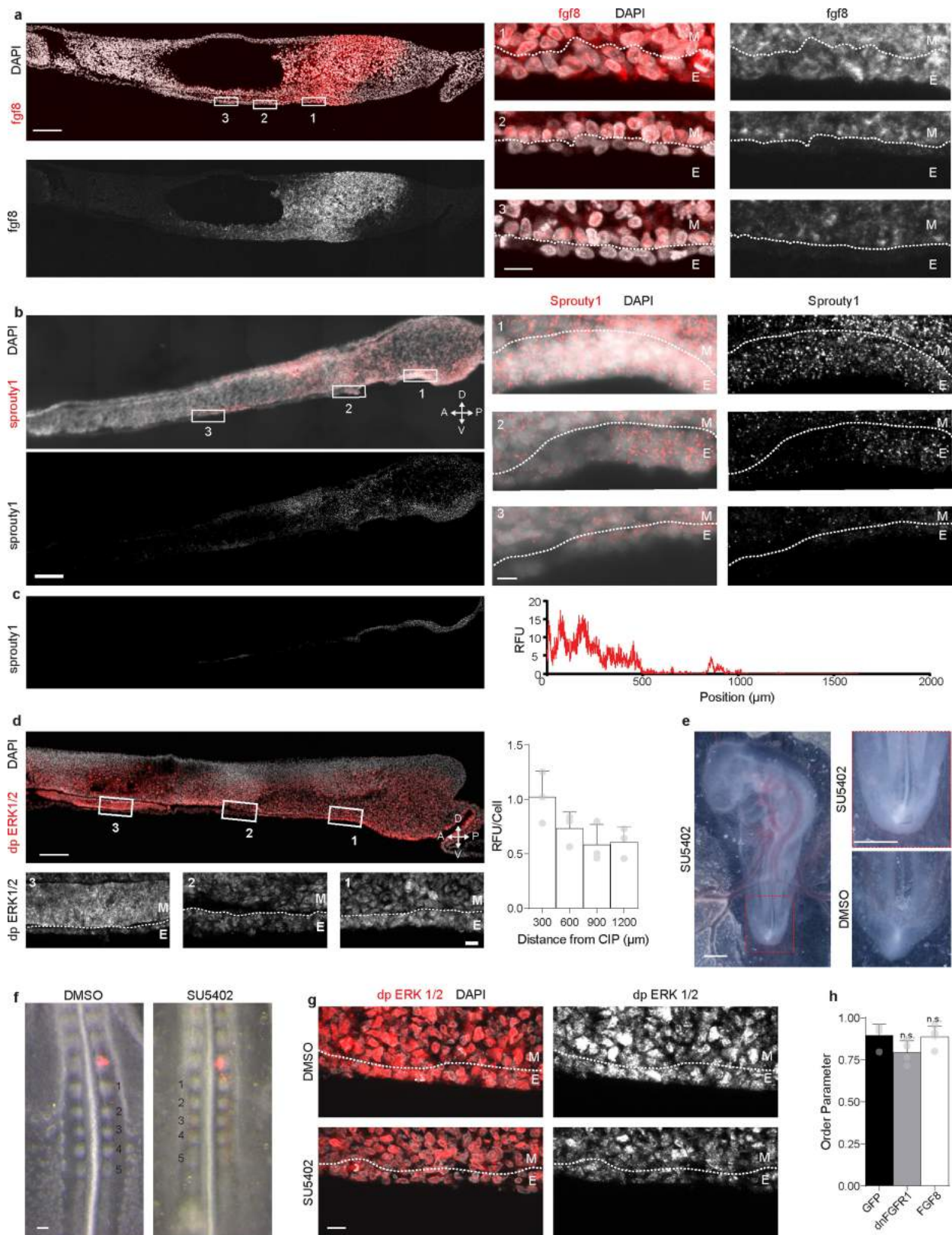
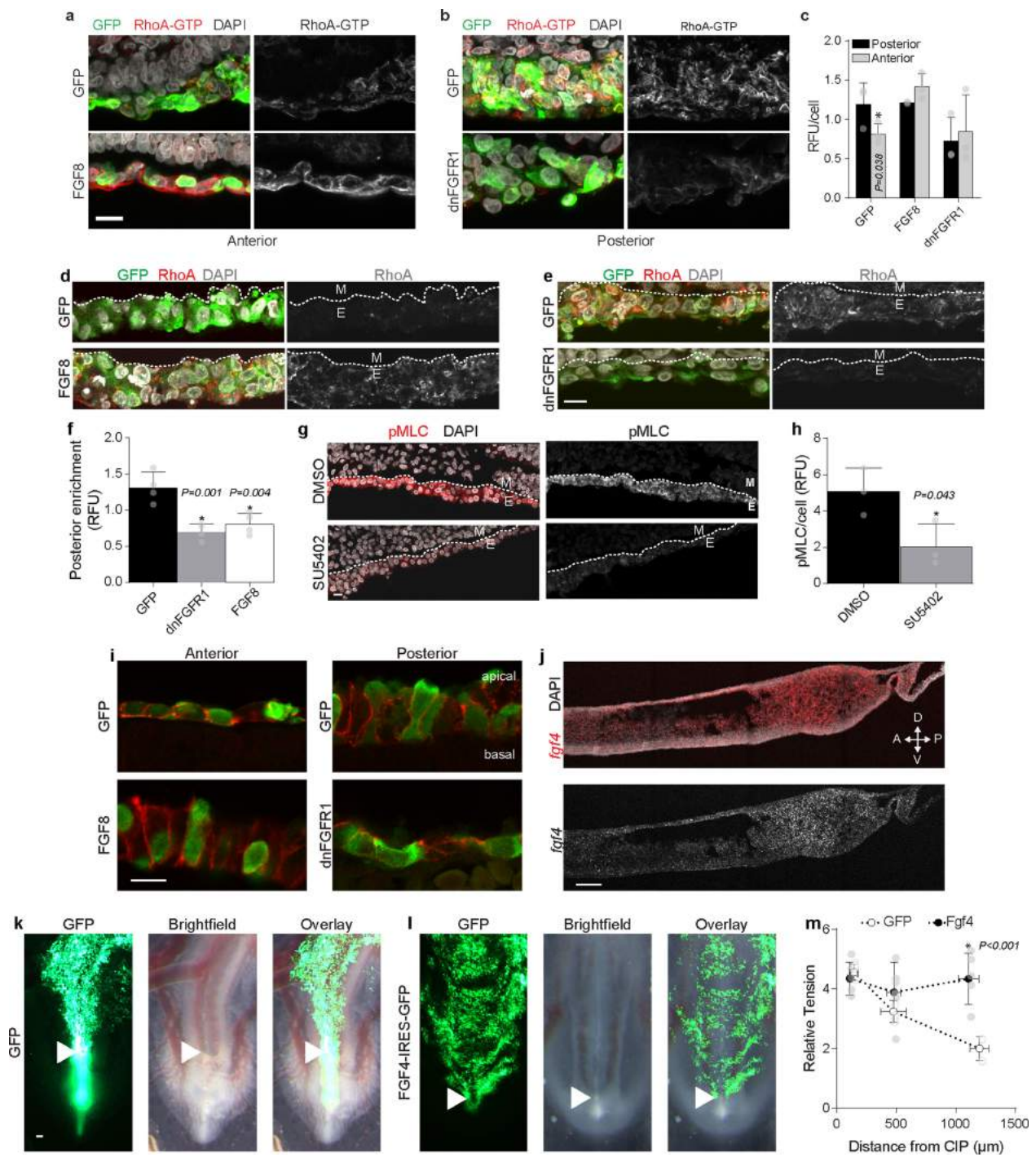**Extended Data Fig 6** | See next page for caption.

Extended Data Fig 6 | FGF signalling in the posterior endoderm. a, **b**, Fluorescent-section in situ hybridization for *FGF8* (**a**) and *sprouty1* (also known as *SPRY1*, **b**) in sagittal sections through the posterior HH15 embryo (left). Numbered boxes indicate regions that are magnified on the right; the dashed line demarcates the boundary between endoderm (E) and mesoderm (M). Scale bars: 100 μm (left), 10 μm (right). Gradient expression of both genes observed in three of three embryos. **c**, Isolated signal from endoderm only (left) and quantification of relative fluorescence (right). **d**, Immunofluorescent detection of di-phospho ERK (dp ERK1/2) with boxed regions magnified below; the dashed line marks the boundary between endoderm (E) and mesoderm (M). Scale bar, 100 μm (top), 10 μm (bottom). Right, quantification of dp ERK1/2 per cell along the antero-posterior axis ($n = 3$ embryos). RFU, relative fluorescent units. **e**, Embryos cultured in the presence of 50 μM SU5402 from HH14 to HH18 (left; outlined region is magnified (top right)) displayed normal anterior development but posterior defects, including axis truncation, allantois malformation and failure of the posterior endoderm to internalize and form hindgut, compared to 0.1% DMSO control (bottom),

$n = 7$ of 9 affected versus 0 of 10 in 0.1% DMSO. Scale bar, 1 mm. **f**, Somitogenesis is unaffected by exposure to 50 μM SU5402 in ex ovo culture, despite dependence of this process on FGF signalling, suggesting that effects of SU5402 were primarily restricted to the endoderm. HH13 embryos were cultured for 9 h in the presence of either 0.1% DMSO or 50 μM SU5402 following DiI injection into the last-formed somite (red) at the time of exposure ($n = 3$). Scale bar, 100 μm. **g**, dp ERK1/2 staining in the posterior endoderm following incubation of embryos from HH13 to HH15 in the presence of either 0.1% DMSO (top, $n = 3$ embryos) or 50 μM SU5402 (bottom, $n = 3$ embryos). Effects of SU5402 were most pronounced in endoderm, with some subtle reduction in dp ERK1/2 extending into the subadjacent mesodermal cells. The white dashed line indicates the boundary between endoderm (E) and mesoderm (M). Scale bar, 10 μm. **h**, Quantification of order parameter for embryos electroporated with GFP, dnFGFR1-IRES-GFP, or FGF8-IRES-GFP. $n = 4$ embryos per condition; data are mean ± s.d.; one-way ANOVA with Tukey's correction; NS, not significant versus GFP.
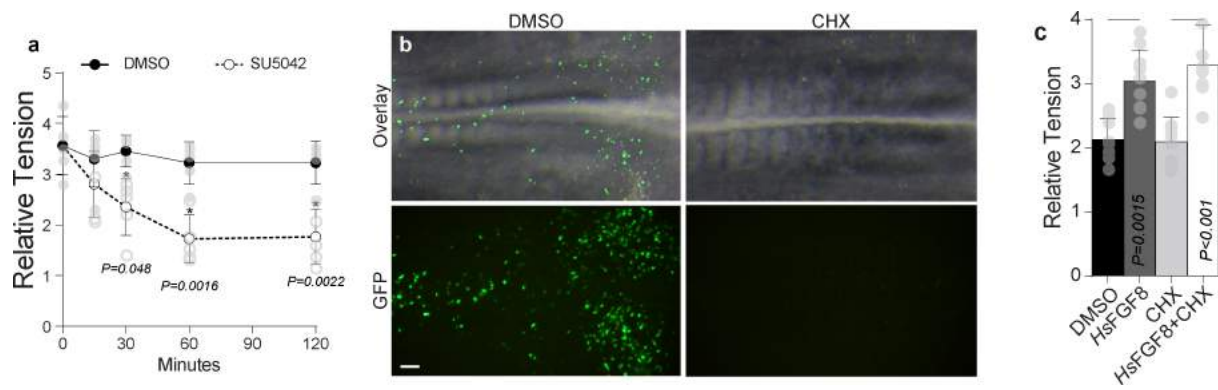
Extended Data Fig. 7 | Role of FGF in modulating endodermal tension via direct effects on actomyosin activity. a, To detect the timescale across which inhibition of FGF signalling induces a reduction in endoderm tension, embryos were exposed to either 0.1% DMSO or 50 μM SU5402 for up to 120 min after onset of exposure, and relative tension was measured over time ($n = 5$ embryos per group per time point). A significant decrease in tension was observed within 30 min of exposure to SU5402. Data are mean ± s.d.; two-way ANOVA with Tukey's correction; *$P < 0.05$ versus DMSO at equivalent time point. **b**, To test efficacy of cycloheximide (CHX) treatment for inhibition of protein translation, embryos were electroporated with GFP and then incubated for 6 h in the presence of either 0.1% DMSO or 20 μM CHX. In contrast to DMSO-treated controls (3 of 3 embryos were GFP$^+$), GFP signal was undetectable in CHX-treated embryos (0 of 3 embryos were GFP$^+$). Scale bar, 100 μm. **c**, Relative tension at HH15 following incubation in 0.1% DMSO or 20 μM CHX in the presence or absence of 500 ng μl^{-1} HsFGF8 ($n = 9$ embryos per condition). Data are mean ± s.d.; one-way ANOVA with Tukey's correction; overbars indicate comparison for stated P value.

Extended Data Fig. 8 | See next page for caption.

Extended Data Fig. 8 | FGF signalling controls tissue strain and contractility in the posterior endoderm. a, b, Sagittal sections ($n = 3$) from HH15 embryos stained with RhoA–GTP and electroporated with GFP or FGF8-IRES-GFP (**a**) in the anterior endoderm, or with GFP or dnFGFR1-IRES-GFP (**b**) in the posterior endoderm. Scale bar, 10 μm. **c,** Quantification of RhoA–GTP immunofluorescence per cell in anterior and posterior endoderm ($n = 3$ embryos per condition). Data are mean ± s.d.; two-way ANOVA with Tukey's correction; *$P < 0.05$ versus posterior. **d, e,** Immunofluorescent detection of total RhoA in HH15 sagittal sections following electroporation with GFP or FGF8-IRES-GFP (**d**) in the anterior endoderm ($n = 4$ embryos), or with GFP or dnFGFR1-IRES-GFP (**e**) in the posterior endoderm ($n = 4$ embryos); the dashed line demarcates the boundary between endoderm (E) and mesenchyme (M). Scale bar, 10 μm. **f,** RhoA enrichment in posterior versus anterior endoderm quantified on a per-cell basis from immunofluorescent detection at HH15 ($n = 4$). Data are mean ± s.d.; one-way ANOVA with Tukey's correction; *$P < 0.05$ versus GFP. **g, h,** Immunofluorescent detection (**g**) and quantification (**h**) of phospho-myosin light chain (pMLC) in the posterior endoderm for embryos cultured from HH13 to HH15 in the presence of either 0.1% DMSO ($n = 3$) or 50 μM SU5402 ($n = 3$); dashed white lines indicate the boundary between endoderm (E) and mesoderm (M). Data are mean ± s.d.; unpaired two-tailed t-test. Scale bar, 10 μm. **i,** To determine whether cell–cell adhesions are altered by FGF signalling, immunofluorescent detection of E-cadherin was carried out in anterior endoderm (left), comparing embryos electroporated with GFP or FGF8-IRES-GFP, and in the posterior endoderm (right), comparing embryos electroporated with GFP or dnFGFR1-IRES-GFP. No overt differences in E-cadherin were observed, with localization along the basolateral boundaries of cells in the posterior and anterior endoderm, independent of FGF activity (in 3 of 3 embryos per condition). Changes in cell morphology are apparent, with FGF8-expressing cells in the anterior endoderm adopting a columnar epithelial morphology similar to that in the wild-type posterior endoderm, and dnFGFR1-expressing posterior endoderm cells becoming flattened, similar to cells in the wild-type anterior endoderm. Scale bar, 10 μm. **j–m,** Owing to redundancy between FGF4 and FG8 in other contexts (see Supplementary Discussion), we tested whether FGF4 and FGF8 act similarly in control of the hindgut-forming endoderm. **j,** Fluorescent section in situ hybridization for *FGF4* in sagittal sections through the posterior HH15 embryo shows a posterior-to-anterior gradient similar to that of *FGF8* (in 3 of 3 embryos). Scale bar, 100 μm. Whole-mount HH18 embryos following electroporation of endoderm at HH12 with GFP (**k**; 0 of 4 affected) or FGF4-IRES-GFP (**l**; 5 of 7 affected) reveals failure of endoderm to internalize and form hindgut upon misexpression of FGF4, phenocopying effects of FGF8 misexpression. Arrowhead, CIP. Scale bar, 100 μm. **m,** Relative tension in HH15 endoderm following electroporation of endoderm with GFP or FGF4-IRES-GFP ($n = 5$ embryos per group) reveals that FGF4, much like FGF8, modulates tension in the posterior endoderm: misexpression eliminates the tensional gradient by elevating tension anteriorly. Data are mean ± s.d.; two-way ANOVA with Tukey's correction; *$P < 0.05$ versus GFP at same antero-posterior level.
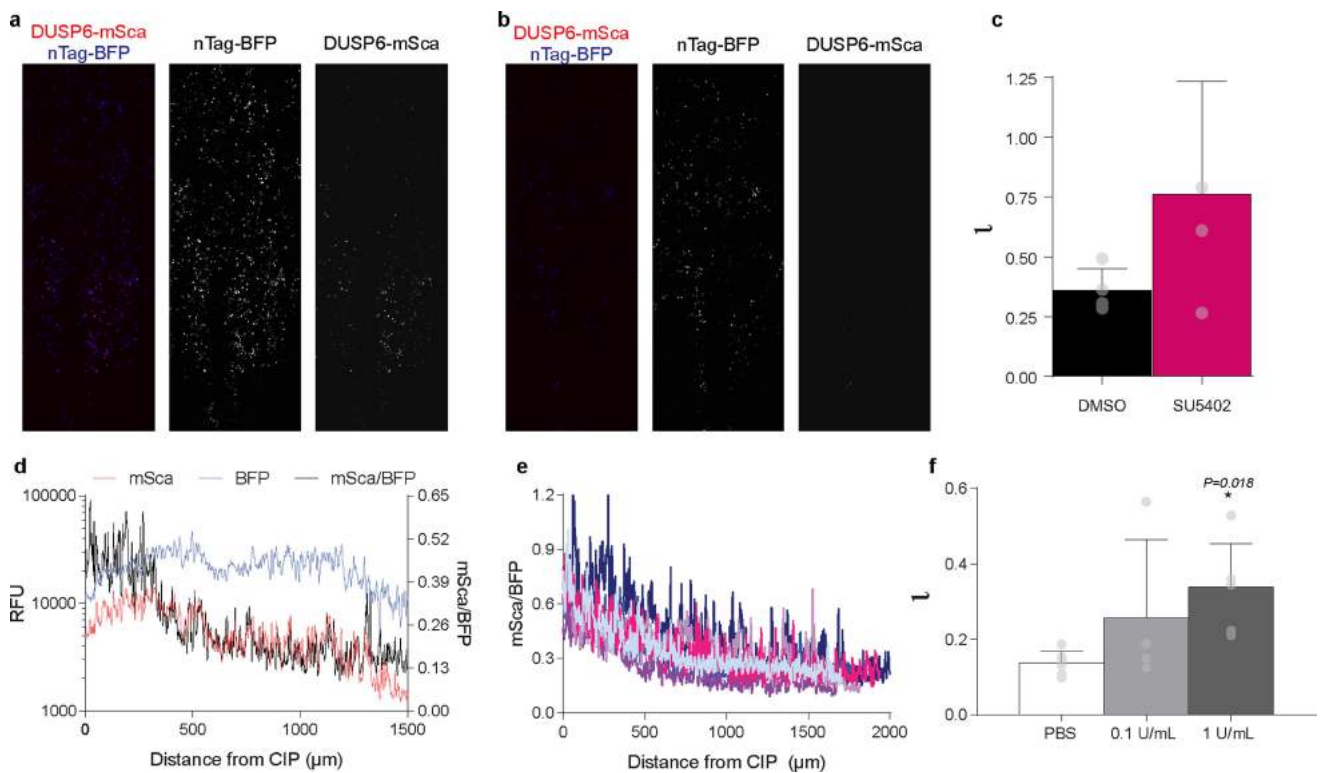
Extended Data Fig. 9 | DUSP6 reporter reveals FGF signalling gradient in posterior endoderm. a–c, DUSP6–mScarlet (mSca) reporter co-electroporated into endoderm with nTagBFP control plasmid in embryos treated with 0.1% DMSO (**a**) or SU5402 (**b**) reveals loss of reporter activity with SU5402 treatment ($n = 4$ embryos). As a result, the FGF signalling gradient was flattened, indicated by quantification of the model and shape parameter ι (**c**). Data are mean $\pm$ s.d.; unpaired two-tailed t-test. **d,** Quantification of DUSP6 reporter-driven mSca activity (red, left y axis), electroporation control nTagBFP signal (blue, left y axis), and the normalized mSca/BFP (black, right y axis) from a single representative embryo (replicates in **e**) as a function of antero-posterior distance from the CIP. **e,** Normalized reporter activity profiles for six wild-type embryos; each embryo denoted by different colour. **f,** To test sensitivity of the DUSP6 reporter to subtle changes in FGF activity (as opposed to the marked effects of FGF ligand misexpression), heparinase I treatment was used to experimentally broaden the gradient. Because FGF ligands are tightly bound by heparin sulfate proteoglycans (HSPGs), treatment to degrade HSPGs would be expected to effectively increase the diffusion coefficient of FGF ligands, resulting in a broadening of the gradient. This effect was confirmed by quantification of the dimensionless FGF-gradient shape parameter ι, as measured by the DUSP6 reporter, following treatment with PBS ($n = 7$ embryos) or heparinase I at 0.1 U ml^{-1} ($n = 4$ embryos) or 1 U ml^{-1} ($n = 6$ embryos). Heparinase caused a dose-dependent increase in ι. Data are mean $\pm$ s.d.;one-way ANOVA with Tukey's correction; *$P < 0.05$ versus PBS.
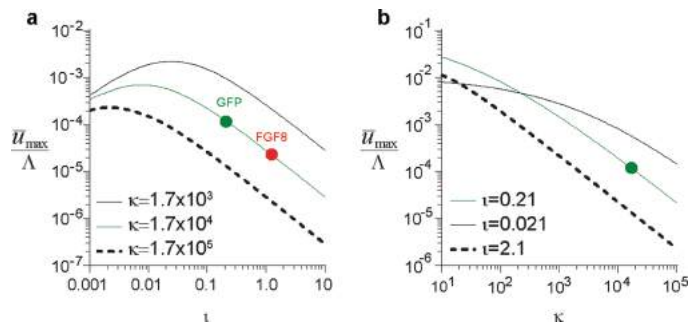
Extended Data Fig. 10 | Parametric evaluation of cell-movement efficiency. Dependence of cell-movement efficiency $\left(\frac{\bar{u}_{max}}{\Lambda}\right)$ on FGF8 transport parameter ι (**a**) and matrix stiffness parameter κ (**b**). Green and red circles indicate experimental values for ι following GFP or FGF8 misexpression, respectively.

In the format provided by the authors and unedited.

Molecular control of macroscopic forces drives formation of the vertebrate hindgut

Nandan L. Nerurkar[1,6,7]*, ChangHee Lee[1], L. Mahadevan[2,3,4,5] & Clifford J. Tabin[1]*

[1]Department of Genetics, Harvard Medical School, Boston, MA, USA. [2]School of Engineering and Applied Sciences, Harvard University, Cambridge, MA, USA. [3]Department of Organismic and Evolutionary Biology, Harvard University, Cambridge, MA, USA. [4]Department of Physics, Harvard University, Cambridge, MA, USA. [5]Kavli Institute for Bionano Science and Technology, Harvard University, Cambridge, MA, USA. [6]Department of Biomedical Engineering, Columbia University, New York, NY, USA. [7]Department of Genetics and Development, Columbia University Medical Center, New York, NY, USA. *e-mail: nln2113@columbia.edu; tabin@genetics.med.harvard.edu

SUPPLEMENTARY INFORMATION

METHODS

Chick embryo culture, labeling, and electroporation

Fertilized White Leghorn chicken eggs (Charles River Laboratories International, Inc.) were incubated at 37.5°C to the desired stage [12], then harvested onto filter paper rings and grown *ex ovo* using the EC method [33]. All experiments were carried out in accordance with protocols approved by the Institutional Animal Care and Use Committee at Harvard Medical School. Vital dye labeling was performed by injection of lipophilic dyes Di I and Di O (2.5 mg/mL in DMF, Invitrogen) using pulled glass capillary needles. To label the entire endoderm, 100 µL PKH26 (1:50 in diluent, Sigma) was applied to the ventral surface of embryos, followed by 5 minutes incubation at room temperature, and then rinsed in PBS to remove unincorporated dye.

The DUSP6-based FGF activity reporter was constructed by subcloning a 508 bp genomic fragment of mouse DUSP6 promoter[34] into a Stagia3 vector[35] modified to include a chimeric intronic sequence to enhance sensitivity (Extended Data Fig. 9) [36]. GFP IRES Alkaline phosphatase was replaced with mScarlet-i fused C-terminally to an H2A nuclear localization sequence[37]. FGF4 and FGF8 misexpression plasmids were generated by cloning mouse *Fgf4* and chick *Fgf8* coding domains into PCAGIG vector. For electroporation, the following plasmids were diluted to 5 – 8 µg/uL in PBS with 5% sucrose and 0.1% Fast Green: GFP, TdTomato, H2B:GFP, dnFGFR1 IRES GFP [27], and FGF8 IRES GFP, FGF4 IRES GFP, each under control of a CAG promoter, and a 1:1 mixture of the DUSP6 reporter and an electroporation control CAG nTagBFP (2.5 µg/uL each); nTagBFP was derived from the modified blue fluorescent protein mTagBFP[38] by insertion into CAG vector and addition of three repeats of the SV40 nuclear localization sequence. HH stage 11 – 12 embryos were submerged in PBS in a dish containing a 2 mm square electrode (+) and covered with PBS[39]. DNA solution was then applied to the ventral surface of embryos, and a second 2mm square electrode (-) was placed approximately 4 mm above the embryo. The following pulse waveform was applied using the Nepa 21 (Nepa Gene, Ichikawa City, Japan): three 40V poring pulses of 0.1 msec duration, separated by 50 msec, with 10% decay between each pulse, followed by five 4V transfer pulses of 5 msec duration, separated by 50 msec, with 40% decay between each pulse. Electroporation of a ubiquitous GFP reporter at HH11-12 resulted in high efficiency GFP expression in the endoderm (Extended Data Fig. 1a-c). Consistent with a posterior shift in endoderm position, electroporations targeting cells at the level of somites 12 – 16 resulted in GFP+ cells at more posterior locations later in development, including throughout the formed hindgut (Extended Data Fig. 1b, c) The number of poring pulses was increased to five for increased efficiency in high magnification time lapse experiments (Fig. 2b and

Supplemental Movie 3), and reduced to a single pulse to increase mosaicism in experiments testing cell autonomy (Fig. 3k). Effects of FGF8 misexpression on FGF activity gradient were assessed by performing two sequences of electroporation, first for co-expression of the DUSP6 reporter and nTagBFP, followed rinsing the embryo in PBS, then performing a second electroporation for either GFP or FGF8 IRES GFP.

Experiments in which acto-myosin contractility was modified to test the effects on cell density, cell shape, and relative tension were performed by incubating HH15 embryos in PBS for 1 hour at 37.5°C in the presence of 5 µM cytochalasin (Tocris), 100 µM Y-27632 (Tocris), 100 µM blebbistatin (Tocris), or 30 nM Calyculin A (Sigma). Notably, higher concentrations or durations of exposure to calyculin A resulted in excessive contraction to the point of endoderm tearing and massive delaimination from the embryo. Therefore, the tension measurements in Fig. 2f) serve as a proof of concept, and are not to be interpreted as an upper limit to contractility or tension measurement. Dependence of FGF-mediated tension on new protein synthesis was tested by incubating HH15 embryos as described above in PBS in the presence of 500 ng/µL recombinant human (rh) FGF8b protein (Invitrogen), and/or 20 µM cycloheximide (Sigma). Translation-blocking was confirmed by electroporation of GFP into HH11 embryos, followed by incubation for 6 hours in PBS containing 20 µM cycloheximide (Sigma, Extended Data Fig. 7b). Time course of SU5402 exposure was performed by incubating embryos in PBS with 50 µM SU5402 at 37.5°C, and revealed that exposure to SU5402 diminished endodermal tension on the timescale of minutes (Extended Data Fig. 7a). To assess the effects of pharmacologic perturbations on hindgut morphogenesis, cytochalasin D, calyculin A, and SU5402 drugs were diluted in molten culture medium to 2.5 µM, 20 nM, and 50 µM, respectively, allowed to set, and then embryos were cultured ventral side down on the culture medium. FGF inhibition by SU5402 exposure was most pronounced in the endoderm (Extended Data Fig. 6e, f), but extended slightly into the subadjacent mesoderm. For bead grafting experiments, heparin agarose beads (McLab Products) were soaked in PBS or 1 mg/mL rhFGF8 (Invitrogen) protein at room temperature for 1 hour, rinsed with PBS, then transferred onto the endoderm. For all pharmacologic studies, 0.1% DMSO by volume was used as the control. The ability of the DUSP6 reporter to resolve subtle changes in FGF activity gradients was confirmed by electroporation of DUSP6-mSca and nTag-BFP as above, followed by incubation with Heparinase I (H2519-50UN, Sigma).

Immunofluorescence and in situ hybridization

To prepare frozen sections, embryos were fixed overnight in 4% paraformaldehyde in DEPC-treated PBS at 4°C, equilibrated sequentially in 10%, 20%, and finally 30% sucrose, then frozen in OCT, and cryosectioned (Leica) to 16 µm thick slices. The following primary antibodies were used: chicken anti-

GFP (1:1,000, ab13970, abcam), rabbit anti-phospho histone H3 (pHH3, 1:300, 06-570, Millipore), mouse anti-laminin (1:100, 3H11, Developmental Studies Hybridoma Bank), mouse anti-Ecadherin (1:100, 610182, BD Biosciences), mouse anti-aPKC Zeta (1:100, sc17781, Santa Cruz), mouse anti-ZO-1 (1:100, 33-9100, Thermo Fisher), rabbit anti-RhoA (1:300, 2117, Cell Signaling), mouse anti-RhoA-GTP (1:100, 26904, New East Biosciences), rabbit anti phospho-myosin light chain (1:300, 3671, Cell Signaling), and rabbit anti di-phospho (dp) ERK 1/2 (1:300, 4376, Cell Signaling). GFP, pHH3, laminin, E-cadherin, aPKC, and ZO-1 were visualized by fluorophore conjugated secondaries (1:500). RhoA-GTP and RhoA antibodies were detected using a horseradish peroxidase (HRP)-conjugated an anti-rabbit secondary antibody (1:500 for 1h at room temperature, 7074, Cell Signaling), followed by 5 minutes incubation with TSA (1:100 in diluent, Perkin Elmer). For pMLC and dpERK1/2, Tris buffered saline was used in place of PBS for all washes, and antibodies were detected using biotinylated anti-rabbit antibody, HRP-conjugated streptavidin (each 1:500 for 1 hour at room temperature,111065003 and 016030084, respectively, Jackson Immuno), and TSA as above. Sections were mounted in Prolong Gold Antifade with DAPI (P36931, Invitrogen) and coverslipped for imaging.

Fluorescent section in situ hybridization was carried out as described previously [40]. Briefly, sagittal sections from HH15 embryos were pretreated for endogenous peroxidase quenching, proteinase K digestion, and acetylation, then hybridized by anti-sense DIG probes transcribed from chick *Fgf8*, *Fgf4*, and *Sprouty1* templates [41–43]. High-stringency washes were performed to remove excess probe, and hybridized probes were detected by anti-DIG-HRP (Roche) antibodies with TSA amplification (1:50 in diluent, 5 – 10 minute incubation).

Imaging

Immunofluorescent sections and fluorescent section in situs were imaged on an inverted LSM710 laser scanning confocal microscope (Zeiss). Whole mount images of stained and/or electroporated chick embryos were collected on a fluorescent stereoscope (M165, Leica). For live imaging, glass bottom culture dishes (Mattek) were coated with a thin layer of semisolid medium as in EC culture [33]. Embryos were electroporated at HH11-12, incubated to HH14, then placed ventral side down on the semisolid medium [44]. Imaging was performed at 10x (unless stated otherwise) on an inverted LSM710 (above) with a heated chamber, and a two-photon Maitai Deepsee titanium sapphire laser (Spectra Physics) was used to visualize cell movements. 850 nm excitation was used to visualize GFP, while 780 nm was used to simultaneously visualize GFP and TdTomato. Z-stacks were collected every 5 minutes. For cell height measurements, GFP-electroporated embryos were imaged

at 20x on a Nikon Ti-E spinning disk confocal microscope, and optical sections along the antero-posterior/dorso-ventral plane were used to measure cell height in midline endoderm.

Analysis of cell movements, biophysical measurements, and image analysis

Tracking of cell movements from time lapse experiments was performed in Imaris (Bitplane), and post processing was performed in MATLAB (MathWorks). From cell positions, Lagrangian strains were calculated. In two dimensions, the strain tensor can be decomposed into local changes in length along two orthogonal axes corresponding to the medio-lateral (x) and antero-posterior (y) embryonic axes (denoted ε_{xx} and ε_{yy}, respectively), and a local change in angle relative to those axes (ε_{xy}, Extended Data Fig. 3a). ε_{xx} and ε_{yy} quantify the degree to which points in a material move toward each other (ε <0, compaction) or away from each other (ε >0, extension) along the x and y axes, respectively (Extended Data Fig. 3a). The conversion of cell displacements to morphogenetic strains has been described previously [19]. Briefly, cell tracks were used to calculate the mediolateral (x-axis) and anteroposterior (y-axis) components of cell displacements at each increment of the time lapse:

$$u_x = u_x(X, Y)$$

$$u_y = u_y(X, Y)$$

Where X and Y are the original, "undeformed" position in the timepoint of the time lapse. A 2-D surface was fit to these data using the Matlab routine gridfit, from which the spatial derivatives were computed and used to calculate Lagranian strain:

$$\boldsymbol{\varepsilon} = \frac{1}{2}(\nabla\boldsymbol{u} + \nabla\boldsymbol{u}^T + \nabla\boldsymbol{u} \cdot \nabla\boldsymbol{u}^T)$$

where $\boldsymbol{\varepsilon}$ is the two-dimensional strain tensor with components ε_{xy} (shearing strain), ε_{xx} (medio-lateral strain), and ε_{yy} (antero-posterior strain), $\boldsymbol{u}$ is the displacement vector, ∇ is the gradient operator, superscript *T* indicates transpose, and · denotes the dot product. Strain analysis of posterior cell movements in the endoderm revealed large shearing strains laterally, but little shearing among the medial endoderm cells that move rapidly from anterior to posterior (Fig. 2c). Along the medio-lateral axis, compaction (ε_{xx} < 0) of cells was observed medially, along with extensional strains (ε_{xx} > 0) laterally (Fig. 2c). At the cellular level, stretching and compaction in a continuous epithelial sheet may be achieved by changes in cell shape or cell-cell contacts that result in an increase or decrease in the distance between neighboring cell centroids, respectively.

Average anteroposterior strain ε_{yy} was calculated by averaging along the x-direction for cells along the midline (approximately 300 um width), extending up to 1,400 um from the CIP. Strain measurements have been used to study a diverse set of problems across various model organisms, including dorsal closure and germband extension in drosophila[45,46], placement (and extension of neuroectoderm in zebrafish[46,47], blastopore closure and gastrulation in xenopus [48], formation of the primitive streak, head fold [19], heart tube and foregut in the chick[19,49,50], and eyelid closure in the mouse [51]. Strain is a mathematical description of how any material changes shape, without any assumptions regarding the material properties, heterogeneities, or activity/inertness of the material. These aspects *are* important in how strain data are interpreted, however. For example, negative strains in an inactive/inert material would likely indicate that the material is under compressive stress, while in an active material, contraction would produce the same negative strains while putting the material into tension instead of compression, as we see in the present work. Stretching and compaction in a continuous epithelial sheet may be achieved by changes in cell shape or cell-cell contacts that result in an increase or decrease in the distance between neighboring cell centroids, respectively**.**

Mean cell velocity was measured as the average total displacement of midline cells divided by the duration of time lapse experiment (8 hours). The order parameter (OP) was calculated as $OP = \left\langle \frac{1}{N} \left| \sum_{i=1}^{N} \frac{\widetilde{v_i}(t_k)}{|\widetilde{v_i}(t_k)|} \right| \right\rangle_{t_k}$ where N is the number of cells tracked, $v_i(t_k)$ is the velocity of cell i at time t_k [52].

Relative tension in the endoderm was measured using a gastromaster with red-tipped probes (Extended Data Fig. 3e-g) to introduce cuts to the endoderm. The gastromaster is an embryological dissection tool in which current is passed through a small platinum wire, ablating tissue it comes into contact with. All experiments were conducted using an 18 μm diameter probe to measure forces on the tissue-scale. The gastromaster probe was mounted on a micromanipulator and brought carefully into contact with the endoderm, and pulsed with current to create tears of reproducible geometry. Embryos in which the cut extended beyond the endoderm to sever the adjacent notochord (Extended Data Fig. 3f) were discarded. Tears in the endoderm sprang open immediately, and remained static for up to a minute (Extended Data Fig.3g) before a wound-response initiated progressive reduction in the size of the tear. Embryos were imaged in <5 seconds following ablation. Relative tension was calculated as the ratio of cut size to probe diameter (Extended Data Fig. 3e).

Proliferation was quantified in whole mount embryos by first electroporating with H2B-GFP and then counterstaining with rabbit-pHH3 (above); colocalization of pHH3 signal with GFP was used distinguish endodermal signal from neighboring tissues, and % dividing cells was quantified by counting the relative proportion of GFP-positive cells that were also pHH3 positive. Cell density was calculated from DAPI stained sagittal sections, and cell shape was measured from ventral views of

GFP-electroporated embryos. FGF activity was quantified in embryos co-electroporated with the DUSP6-mScarlet reporter and an nTagBFP control: mScarlet intensity was normalized to BFP, then summed medio-laterally to provide a readout of FGF along the antero-posterior axis (Extended Data Fig. 9d). RhoA-GTP enrichment was quantified from sagittal sections of HH15 embryos by taking the summed total pixel intensity divided by the number of cells in posterior (0 – 300 μm from the CIP) and antertior (600 – 900 μm from the CIP) endoderm. Total RhoA enrichment was measured similarly, but with normalization of anterior to posterior signal enrichment on a per embryo basis to account for the high sample to sample variability. pMLC and dp ERK 1/2 were measured using the same approach.

Statistical Analyses

In all plots, center values are the mean and error bars represent standard deviations from the mean, each from biological replicates. All statistical tests were performed using GraphPad Prism 6. Dependence on position was determined by Pearson's correlation, and P values were obtained from either one or two way ANOVAs with Tukey's Post hoc correction for multiple comparisons. Among each compared groups, the degree of variance was similar. No statistical methods were used to determine sample size prior to experiments. Embryos were excluded from further analysis if electroporation-dependent malformations (e.g. holes burned into endoderm) were observed, if electroporation efficiencies were too low (below ~30-50%), if excessive drift occurred during time lapse experiments, or if gastromaster-induced tears extended beyond the endoderm into neighboring notochord or presomitic mesoderm. No randomization or blinding was employed for processing samples.

Mathematical model of FGF-mediated contractile gradient based cell movements

Given the observations that FGF activity is correlated with active cellular contractility, we turn to a minimal one dimensional mathematical model to understand how transport properties of a diffusible modulator of contractility, FGF ligand, and cell contractility combine to regulate cell movements. The model is related to a broad class of chemo-mechanical theories of active matter and morphogenesis in other contexts [53,54] that links biochemical activity and diffusion to force generation.

Formulation

For simplicity, the endoderm is treated as a one-dimensional active linear viscoelastic solid. The passive stress σ_p is described by a Kelvin-Voigt constitutive law of the form:

$$\sigma_p = E\varepsilon + \eta\frac{\partial\varepsilon}{\partial t} = E\frac{\partial u}{\partial y} + \eta\frac{\partial^2 u}{\partial t\partial y} \qquad (1)$$

where E and η are the Young's modulus and viscosity of the endoderm, respectively, and strain $\varepsilon = \frac{\partial u}{\partial y}$, the derivative of the displacement u, with respect to position along the endoderm, y. The active stress – resulting from acto-myosin contractions denoted σ_a – is assumed to be proportional to FGF8 concentration, [FGF8]:

$$\sigma_a = \alpha[FGF8] \qquad (2)$$

where α is a proportionality constant with dimensions of stress. The total stress in the system is the sum of (1) and (2) and given by:

$$\sigma = \sigma_p + \sigma_a = E\frac{\partial u}{\partial y} + \eta\frac{\partial^2 u}{\partial t\partial y} + \alpha[Fgf8] \qquad (3)$$

We note that at short times, the stress is dominated by its viscous component, while at long times, it is dominated by its elastic component, consistent with the observed behavior that the tissue is elastic at long times/long length scales but behaves like a fluid on short length scales/times owing to cellular movements. Since FGF8 is a secreted protein, it diffuses with a diffusion coefficient D from a source of constant concentration at $y=0$, corresponding to the posterior end of the endoderm. We assume further that there is a uniform and constant degradation rate R_d, representing turnover and clearing of FGF8-bound receptors and extracellular degradation. Then, assuming that the contribution to FGF8 concentration from cellular advection is negligible, the equation that governs [FGF8] concentration is given by:

$$\frac{\partial[FGF8]}{\partial t} = D\frac{\partial^2[FGF8]}{\partial y^2} - R_d[FGF8] \qquad (4)$$

This source-sink model is consistent with the observed distribution of FGF reporter activity (Fig. 3a-c), and the morphogenic activity of FGF8 in other contexts[30]. Assuming that FGF8 concentration equilibrates rapidly relative to cell movements (D ~ 50 – 90 µm²s⁻¹ as described by Yu et al), we approximate the concentration of FGF8 as its steady state, i.e. $\frac{\partial[FGF8]}{\partial t} = 0$ [30]. A natural length scale that arises from (4), due to the balance between diffusion and degradation is given by $\sqrt{D/R_d}$ which we assume is smaller than the length of the presumptive hindgut L. Adopting a coordinate system in which the y-axis lies along the embryonic antero-posterior axis, with the origin at the posterior end (i.e. the CIP), and the proximal boundary condition [FGF8]$_{y=0}$ = C_o, the steady state concentration of FGF8 as a function of antero-posterior position is given by:

$$[FGF8] = C_o e^{-\frac{y}{\sqrt{D/R_d}}} \tag{5}$$

Substituting (5) into (3) gives:

$$\sigma = \sigma_p + \sigma_a = E\varepsilon + \eta\frac{\partial\varepsilon}{\partial t} = E\frac{\partial u}{\partial y} + \eta\frac{\partial^2 u}{\partial t \partial y} + \alpha C_o e^{-\frac{y}{\sqrt{D/R_d}}} \tag{6}$$

The dynamics of slow elongation of the hindgut (ignoring any inertial effects) may then be written as

$$\frac{\partial\sigma}{\partial y} + f_b = 0 \tag{7}$$

where f_b is the resistance to deformation from the basement membrane. We model this resistance as a simple linear elastic force, writing $f_b = -k_{ecm}u$. Substituting this, along with (6) into (7) provides:

$$E\frac{\partial^2 u}{\partial y^2} + \eta\frac{\partial^3 u}{\partial t \partial y^2} - k_{ecm}u = \frac{\alpha C_o}{\sqrt{D/R_d}}e^{-\frac{y}{\sqrt{D/R_d}}} \tag{8}.$$

subject to the boundary conditions $u(0,t) = u(L,t)=0$; L is assumed to be large relative to the diffusion length of FGF, in order to minimize the effects of this simplification on cell movements. Furthermore, we assume that $u(y,0)=0$ as the initial condition. Together with these conditions, (8) presents a mixed third order linear partial differential equation to be solved for $u(y,t)$.

Non-dimensionalizing the partial differential equation

Introducing the following nondimensional variables $\bar{y} = \frac{y}{L}$, $\bar{u} = \frac{u}{L}$, $\bar{t} = \frac{E}{\eta}t$

and substituting into (8), with some rearrangement, the resulting equation can be further simplified upon introduction of three dimensionless parameters: $\iota = \frac{\sqrt{D/R_d}}{L}$, $\kappa = \frac{k_{ecm}L^2}{E}$, $\Lambda = \frac{\alpha C_o}{E}$.

Each of these parameters has a clear physical interpretation: ι is a ratio of the characteristic length scale of the transport problem to the length scale of the endoderm, κ is a ratio of extracellular matrix stiffness to cell stiffness, and Λ is the ratio of active contractile stress to cell stiffness. The differential equation (8) can now be rewritten in a form that depends only on these 3 dimensionless parameters (ι, κ, and Λ) instead of the original 8 (E, η, α, k_{ecm}, L, D, R_d, and C_o):

$$\frac{\partial^2 \bar{u}}{\partial \bar{y}^2} + \frac{\partial^3 \bar{u}}{\partial \bar{t} \partial \bar{y}^2} - \kappa \bar{u} = \frac{\Lambda}{\iota} e^{-\frac{\bar{y}}{\iota}} \tag{9}$$

with boundary conditions given by $\bar{u}(0, \bar{t}) = \bar{u}(1, \bar{t}) = 0$, and initial condition $\bar{u}(\bar{y}, 0) = 0$. Notably, endoderm viscosity η is entirely absorbed into the scaled time variable $\bar{t}$ and therefore does not appear explicitly in (9). This suggests that viscosity does not change the behavior of the system, but serves to scale the time variable instead.

Solving and implementing the model

The partial differential equation (9) is a linear initial boundary value problem, and because the spatial variable $\bar{y}$ is finite ($0 \le \bar{y} \le 1$), an exact solution can be obtained using the Finite Fourier Transform approach[55]. Using the basis of the form $\Phi_n = \sin n\pi \bar{y}$, we can transform (9) into an ordinary differential equation for the spectral coefficients $u_n(\bar{t})$, with the result in an infinite sum of the form:

$$\bar{u}(\bar{y}, \bar{t}) = \sum_{n=1}^{\infty} \Lambda \frac{n\pi \iota (e^{-\frac{1}{\iota}}(-1)^n - 1)}{((n\pi)^2 + \kappa)(1 + (n\pi\iota)^2)} \left[1 - e^{-\frac{(n\pi)^2 + \kappa}{(n\pi)^2} \bar{t}} \right] \sin n\pi \bar{y} \tag{10}$$

The solution (10) was used in MATLAB to perform calculations and simulations of contractile gradient behavior. The first several terms of the series were used to account for a wide range of parameter values, as when ι was very small or κ was very large, fewer terms led to damped oscillatory behaviors. The value of ι was determined by fitting the scaled solution of the transport problem by least-squares to experimental DUSP6 reporter data for FGF activity vs. antero-posterior position.

SUPPLEMENTAL DISCUSSION

Contractile gradients as a conserved morphogenetic mechanism in epithelia

In the present work, we identified a collective polarized movement of endoderm cells that is essential for hindgut formation, and determined that these movements arise through an FGF-mediated cell contraction gradient. Contractile/strain gradients have been observed in other contexts, primarily in drosophila, suggesting that this may be a highly conserved morphogenetic mechanism of collective cell movement in an epithelium. For example, observations consistent with a contractile/force gradient have been established in ventral furrow formation [56,57] and dorsal closure [45]. However, it is unclear whether these examples also rely on the conversion of a diffusible signal into a mechanical force gradient, as we observe in the present study. On the contrary, the contractile gradient driving ventral

furrow formation is established by a signaling gradient downstream of expression of the transcription factor *twist*, which in turn in transcribed in response to a maternally deposited transcription factor [58]. Nonetheless, from the mechanical stand point, there are many similarities. For example, in both ventral furrow and the posterior chick endoderm, larger forces are seen perpendicular to the direction of collective cell movements (Extended Data Fig. 3j).

Actomyosin force generation and collective epithelial cell movements during embryonic development

The cellular mechanisms at work downstream of FGF signaling in the endoderm resemble those of other events in the chick embryo, such as gastrulation and neurulation [49,59,60]. The critical difference is that in the latter two examples, contractility is anisotropic (directionally biased), and therefore results in cellular reorganization via intercalary cell movements. On the other hand, in the endoderm, a spatial gradient in the degree of *isotropic* contraction results in collective movements without medio-lateral reorganization. Such collective cell movements are prevalent throughout development. In most commonly studied examples, such as migration of the zebrafish lateral line, the propulsive force for cell movements is provided by a "leader" population of cells that undergo a partial epithelial to mesenchymal transition, directionally extending protrusions and pulling follower cells along as a rigid, nondeforming body [18,22,61,62]. This is in contrast to our findings in the posterior endoderm, where large compaction strains and a reduction in cell area coincide with increased tensile forces. Although the physical mechanism of cell movements in the endoderm is distinct from lateral line migration, it is interesting that molecularly, FGF signaling is critical for both processes [22,26,63]. Indeed the role of FGF and its downstream effectors in collective cell movements, and tube elongation in particular, is highly conserved across species and tissues [64–69]. Whether the effects on physical forces that drive morphogenesis are similar or distinct in each of these systems is unclear.

The role of cell-cell adhesion during collective cell movements

The present work provides a molecular link between FGF activity and tissue-level forces in the posterior endoderm. We show that the cellular mechanism depends, to some extent, on RhoA activity upstream of actomyosin contraction and cell shape changes. One distinct, yet complementary alternative mechanism could potentially be through changes in cell adhesion. An important role for E-cadherin in collective cell migration [70] and epithelial morphogenesis[71] has been described in other contexts [72]. However, we observed no differences in E-Cadherin, the main cell adhesion molecule

expressed in these epithelial cells, along the antero-posterior axis (Extended Data Fig. 2b), nor any changes in E-Cadherin levels following misexpression of dnFGFR1 or FGF8 (Extended Data Fig. 8f). This is in contrast to phospho-myosin light chain in the posterior endoderm, which was significantly reduced following SU5402 treatment (Extended Data Fig. 8d, e). However, because contractility and cell-cell adhesion are inextricably linked by the balance of intra- and inter-cellular forces [73,74], we cannot rule out a potential role for FGF-mediated control of cell adhesion in controlling cell movements. Moreover, while FGF signaling controls endoderm tension through acto-myosin dependent cell shape changes, how contractility yields these changes at the subcellular level remains unclear.

Linking molecular cues to mechanical force gradients

The present work focuses largely on the role of FGF8 in posterior morphogenesis of the hindgut. However, in the neighboring mesoderm, FGF4, which is also expressed in a postero-anterior gradient (Extended Data Fig. 8g), has been shown to act redundantly with FGF8 [75–77]. We therefore tested whether a similar redundancy exists in the endoderm by electroporation-based misexrpression of *Fgf4.* Similar to the posterior mesoderm, *Fgf4* misexpression phenocopied *Fgf8,* causing failure of endoderm to internalize and form hindgut (Extended Data Fig. 8h-i). Measurement of relative tension revealed that the disruption of cell movements coincided with a loss in the tensional gradient due to elevation of anterior tension in the endoderm (Extended Data Fig, 8j), similar to the effects of *Fgf8* (Fig. 3g). Therefore, it is likely a gradient in FGF activity, and not a single FGF ligand, that establishes the tensional gradient. Although we show that FGF signaling is necessary and sufficient to modulate the tensional gradient driving hindgut formation, other signaling pathways such as Wnt and retinoic acid are also graded along the antero-posterior axis [78]. What, if any, role these pathways play in controlling cell movements in the endoderm will be investigated in future work. Finally, while *Fgf8* is broadly expressed in a posterior to anterior gradient in the mesoderm, it is also expressed in the posterior endoderm itself, in a much more restricted domain (Extended Data Fig. 6a). To what extent mesodermal vs. endodermal FGF8 production contributes to the control of cell movements remains unclear. The redundancy with FGF4, and the dependence of both hindgut formation and posterior extension of the elongating embryo on the same gradient of FGF ligand make this a difficult problem to tease out.

11

Mathematical modeling of collective cell movements

Once the mathematical model (formulation detailed in Methods) was validated by prediction of the FGF8 overexpression phenotype (Fig. 4D), we next performed simulations to determine how each parameter influences the efficiency of cell movements *in silico*. For these purposes, efficiency was defined as the ratio of the maximal displacement $\bar{u}_{max}$ (output) to contractility Λ (input). Efficiency was strongly and nonlinearly dependent on the FGF transport parameter ι (green curve, Extended Data Fig. 10a). If ι were too small, indicating a sharp, local gradient of FGF activity, efficiency of cell movements would be low due to the relatively few posterior cells actively contracting (Extended Data Fig. 10a). Alternatively, a broader FGF gradient (for example due to an increase in diffusivity or reduction in clearance of FGF ligand), cells throughout the endoderm would contract, and the directional bias that drives cell movements would be diminished. This is analogous to the *Fgf8* misexpression experiments (red dot, Extended Data Fig. 10a), wherein expanding the signaling gradient led to an increase in anterior tension accompanied by a reduction in cell movements (Fig. 3 and Supplemental Movie 6). As κ increases (i.e. an increase extracellular matrix stiffness relative to endoderm stiffness), the optimal value for ι increases as well, indicating that the diffusible signal must act over progressively longer distances to overcome an increase in extracellular matrix stiffness. Finally, we tested how efficiency of cell movements depends on the stiffness ratio κ (Extended Data Fig. 10b). While small values of κ (i.e. soft extracellular matrix and/or stiff cells) had little effect on efficiency (green curve, Extended Data Fig. 10b), at higher values efficiency decreased rapidly with increasing κ. How strongly κ influenced the efficiency of cell movements was directly dependent on the shape of the FGF gradient: as the gradient acts over progressively larger regions, the effects of κ become more pronounced.

SUPPLEMENTAL REFERENCES

33.	Chapman, S. C., Collignon, J., Schoenwolf, G. C. & Lumsden, A. Improved method for chick whole-embryo culture using a filter paper carrier. *Dev. Dyn.* **220,** 284–289 (2001).

34.	Ekerot, M. *et al.* Negative-feedback regulation of FGF signalling by DUSP6/MKP-3 is driven by ERK1/2 and mediated by Ets factor binding to a conserved site within the DUSP6/MKP-3 gene promoter. *Biochem. J* **412,** 287–298 (2008).

35. Emerson, M. M. & Cepko, C. L. Identification of a retina-specific Otx2 enhancer element active in immature developing photoreceptors. *Dev. Biol.* **360,** 241–255 (2011).

36. Brondyk, W. H. pCl and pSI Mammalian Expression Vectors. *Promega Notes* **44,** (1994).

37. Bindels, D. S. *et al.* mscarlet: a bright monomeric red fluorescent protein for cellular imaging. *Nat. Publ. Gr.* **14,** (2016).

38. Subach, O. M. *et al.* Conversion of Red Fluorescent Protein into a Bright Blue Probe. *Chem. Biol.* **15,** 1116–1124

39. Fukuda, K. Electroporation of Nucleic Acids into Chick Endoderm Both In Vitro and In Ovo. in *Electroporation and Sonoporation in Developmental Biology* 73–83 (Springer Japan, 2009). doi:10.1007/978-4-431-09427-2_8

40. Shyer, A. E. *et al.* Bending Gradients : How the Intestinal Stem Cell Article Bending Gradients : How the Intestinal Stem Cell Gets Its Home. *Cell* **161,** 569–580 (2015).

41. Niswander, L., Jeffrey, S., Martin, G. R. & Tickle, C. A positive feedback loop coordinates growth and patterning in the vertebrate limb. *Nature* **371,** 609–612 (1994).

42. Delfini, M.-C. *et al.* The timing of emergence of muscle progenitors is controlled by an FGF/ERK/SNAIL1 pathway. *Dev. Biol.* **333,** 229–237 (2009).

43. Brent, A. E., Schweitzer, R. & Tabin, C. J. A somitic compartment of tendon progenitors. *Cell* **113,** 235–48 (2003).

44. Gros, J., Feistel, K., Viebahn, C., Blum, M. & Tabin, C. J. Cell movements at Hensen's node establish left/right asymmetric gene expression in the chick. *Science* **324,** 941–944 (2009).

45. Gorfinkiel, N., Blanchard, G. B., Adams, R. J. & Martinez Arias, A. Mechanical control of global cell behaviour during dorsal closure in Drosophila. *Development* **136,** 1889–1898 (2009).

46. Blanchard, G. B. *et al.* Tissue tectonics: morphogenetic strain rates, cell shape change and intercalation. *Nat. Methods* **6,** 458–464 (2009).

47.   Smutny, M. *et al.* Friction forces position the neural anlage. *Nat. Cell Biol.* **19,** 306–317 (2017).

48.   Feroze, R., Shawky, J. H., von Dassow, M. & Davidson, L. A. Mechanics of blastopore closure during amphibian gastrulation. *Dev. Biol.* **398,** 57–67 (2015).

49.   Voiculescu, O., Bertocchini, F., Wolpert, L., Keller, R. E. & Stern, C. D. The amniote primitive streak is defined by epithelial cell intercalation before gastrulation. *Nature* **449,** 1049–1052 (2007).

50.   Hosseini, H. S., Garcia, K. E. & Taber, L. A. A new hypothesis for foregut and heart tube formation based on differential growth and actomyosin contraction. *Development* **144,** 2381–2391 (2017).

51.   Heller, E., Kumar, K. V., Grill, S. W. & Fuchs, E. Forces generated by cell intercalation tow epidermal sheets in mammalian tissue morphogenesis. *Dev. Cell* **28,** 617–32 (2014).

52.   Szabó, B. *et al.* Phase transition in the collective migration of tissue cells: Experiment and model. *Phys. Rev. E - Stat. Nonlinear, Soft Matter Phys.* **74,** 1–5 (2006).

53.   Taber, L. A. Pattern Formation in a Nonlinear Membrane Model for Epithelial Morphogenesis. *Acta Biotheor.* **48,** 47–63 (2000).

54.   Murray, J. D. *Mathematical Biology*. **18,** (Springer-Verlag, 1993).

55.   Deen, W. M. *Analysis of Transport Phenomena*. (Oxford University Press, Inc., 1998).

56.   Martin, A. C., Gelbart, M., Fernandez-Gonzalez, R., Kaschube, M. & Wieschaus, E. F. Integration of contractile forces during tissue invagination. *J. Cell Biol.* **188,** 735–749 (2010).

57.   Rauzi, M. *et al.* Embryo-scale tissue mechanics during Drosophila gastrulation movements. *Nat. Commun.* **6,** 8677 (2015).

58.   Heer, N. C. *et al.* Actomyosin-based tissue folding requires a multicellular myosin gradient. *Development* **144,** 1876–1886 (2017).

59.   Nishimura, T., Honda, H. & Takeichi, M. Planar cell polarity links axes of spatial dynamics in

neural-tube closure. *Cell* **149,** 1084–97 (2012).

60. Rozbicki, E. *et al.* Myosin-II-mediated cell shape changes and cell intercalation contribute to primitive streak formation. *Nat. Cell Biol.* **17,** 397–408 (2015).

61. Mayor, R. & Etienne-manneville, S. The front and rear of collective cell migration. *Nat. Publ. Gr.* **17,** 97–109 (2016).

62. Rørth, P. Collective Cell Migration. *Annu. Rev. Cell Dev. Biol.* **25,** 407–429 (2009).

63. Durdu, S. *et al.* Luminal signalling links cell communication to tissue architecture during organogenesis. *Nature* **515,** 120–4 (2014).

64. Sutherland, D. & Samakovlis, C. branchless Encodes a Drosophila FGF Homolog That Controls Tracheal Cell Migration and the Pattern of Branching. *Cell* **87,** 1091–1101 (1996).

65. Atsuta, Y. & Takahashi, Y. FGF8 coordinates tissue elongation and cell epithelialization during early kidney tubulogenesis. *Development* **142,** 2329–2337 (2015).

66. Makarenkova, H. P. *et al.* Differential interactions of FGFs with heparan sulfate control gradient formation and branching morphogenesis. *Sci. Signal.* **2,** ra55 (2009).

67. Morita, K. & Nogawa, H. EGF-dependent lobule formation and FGF7-dependent stalk elongation in branching morphogenesis of mouse salivary epithelium in vitro. *Dev. Dyn.* **215,** 148–54 (1999).

68. Steinberg, Z. FGFR2b signaling regulates ex vivo submandibular gland epithelial cell proliferation and branching morphogenesis. *Development* **132,** 1223–1234 (2005).

69. Huebner, R. J., Neumann, N. M. & Ewald, A. J. Mammary epithelial tubes elongate through MAPK-dependent coordination of cell migration. **2,** 983–993 (2016).

70. Cai, D. *et al.* Mechanical feedback through E-cadherin promotes direction sensing during collective cell migration. *Cell* **157,** 1146–59 (2014).

71. Wang, Y.-C., Khan, Z., Kaschube, M. & Wieschaus, E. F. Differential positioning of adherens

junctions is associated with initiation of epithelial folding. *Nature* **484,** 390–393 (2012).

72. Halbleib, J. M. & Nelson, W. J. Cadherins in development: cell adhesion, sorting, and tissue morphogenesis. *Genes Dev.* **20,** 3199–214 (2006).

73. Parsons, J. T., Horwitz, A. R. & Schwartz, M. a. Cell adhesion: integrating cytoskeletal dynamics and cellular tension. *Nat. Rev. Mol. Cell Biol.* **11,** 633–643 (2010).

74. Guillot, C. & Lecuit, T. Mechanics of epithelial tissue homeostasis and morphogenesis. *Science* **340,** 1185–9 (2013).

75. Naiche, L. A., Holder, N. & Lewandoski, M. FGF4 and FGF8 comprise the wavefront activity that controls somitogenesis. *Proc. Natl. Acad. Sci. U. S. A.* **108,** 4018–23 (2011).

76. Boulet, A. M. & Capecchi, M. R. Signaling by FGF4 and FGF8 is required for axial elongation of the mouse embryo. *Dev. Biol.* **371,** 235–45 (2012).

77. Sun, X., Mariani, F. V. & Martin, G. R. Functions of FGF signalling from the apical ectodermal ridge in limb development. *Nature* **418,** 501–508 (2002).

78. Aulehla, A. & Pourquié, O. Signaling gradients during paraxial mesoderm development. *Cold Spring Harb. Perspect. Biol.* **2,** a000869 (2010).